Full Title

Actin and an unconventional myosin motor, TgMyoF control the organization and dynamics of the endomembrane network in *Toxoplasma gondii*.

Short Title

Endomembrane dynamics in *Toxoplasma gondii*

Authors

Romain Carmeille[1], Aoife T. Heaslip[1]*

Affiliations

[1]Department of Cell and Molecular Biology, University of Connecticut, Storrs, CT, 06269, USA

*Corresponding Author
Email: aoife.heaslip@uconn.edu (AH)

Abstract

Toxoplasma gondii is an obligate intracellular parasite that relies on three distinct secretory organelles, the micronemes, rhoptries and dense granules, for parasite survival and disease pathogenesis. Secretory proteins destined for these organelles are synthesized in the endoplasmic reticulum (ER) and sequentially trafficked through a highly polarized endomembrane network that consists of the Golgi and multiple post-Golgi compartments. Currently, little is known about how the parasite cytoskeleton controls the positioning of the organelles in this pathway, or how vesicular cargo is trafficked between organelles. Here we show that F-actin and an unconventional myosin motor, TgMyoF, control the dynamics and organization of the organelles in the secretory pathway, specifically ER tubule movement, apical positioning of the Golgi and post-Golgi compartments, apical positioning of the rhoptries and finally, the directed transport of Rab6-positive and Rop1-positive vesicles. Thus, this study identifies TgMyoF and actin as the key cytoskeletal components that organize the endomembrane system in *T. gondii*.

Author Summary

Endomembrane trafficking is a vital cellular process in all eukaryotic cells. In most cases the molecular motors myosin, kinesin and dynein transport cargo including vesicles, organelles and transcripts along actin and microtubule filaments in a manner analogous to a train moving on its tracks. For the unicellular eukaryote *Toxoplasma gondii*, the accurate trafficking of proteins through the endomembrane system is vital for parasite survival and pathogenicity. However, the mechanisms of cargo transport in this parasite are poorly understood. In this study, we fluorescently labeled multiple endomembrane organelles and imaged their movements using live cell microscopy. We demonstrate that filamentous actin and an unconventional myosin motor named TgMyoF control both the positioning of organelles in this pathway and the movement of transport vesicles throughout the parasite cytosol. This data provides new insight into the mechanisms of cargo transport in this important pathogen and expands are understanding of the biological roles of actin in the intracellular phase of the parasite's growth cycle.

Introduction

Toxoplasma gondii is a member of the phylum Apicomplexa, which contains over 5000 species of parasites that cause substantial morbidity and mortality worldwide (1,2). *T. gondii* can cause life-threatening disease in immunocompromised individuals and when infection occurs in utero (3–5). Additionally, *T. gondii* is estimated to cause persistent life-long infection in 10-70% of the world's population depending on geographic location (6).

T. gondii is an obligate intracellular parasite, and thus parasite survival and disease pathogenesis rely on the parasite's lytic cycle involving host cell invasion, parasite replication within a specialized vacuole termed the parasitophorous vacuole (PV), and host cell egress that results in destruction of the infected cells (reviewed by (7)). To complete this lytic cycle, the parasite relies on three specialized secretory organelles, the micronemes, rhoptries, and dense granules. Micronemes are small vesicles that are localized predominately at the parasite's apical end (8) and are important for parasite motility, attachment and initiating invasion (Reviewed by (9)). Rhoptries are larger club shaped organelles that contain two sub-sets of proteins (rhoptry bulb proteins (ROPs) and rhoptry neck proteins (RONs)) categorized based on their functions and location within the rhoptry (10). After initial attachment to the host cell, RONs contribute to the formation of the moving junction, a ring structure that aids in the propulsion of the parasite into the host cell (11–15). Once invasion is initiated ROPs and dense granule proteins (GRAs) are secreted into the host cell where they control the organization and structure of the PV, and modulate host gene expression and immune response pathways (10,16–18).

Secretory proteins destined for these distinct organelles are synthesized in the endoplasmic reticulum (ER) and must sequentially traverse multiple intermediate compartments within *T. gondii's* highly polarized endomembrane system before ultimately arriving at their final destination. Newly synthesized proteins are first trafficked to the Golgi which is located adjacent to the nucleus at the parasite's apical end. Dense granules are formed from post-Golgi vesicles (19,20) while proteins destined for the micronemes and rhoptries are trafficked through one or more post-Golgi compartments (PGCs), although the exact route taken by each secretory protein has not been elucidated and the function of each PGC has not been fully defined (Fig. 1a). Two of these compartments are marked by Rab5a and Rab7 and are referred to as the endosome-like compartments, as these proteins are markers of the early and late endosomes in higher eukaryotes (21). While the function of the Rab7 compartment is not known (22), overexpression of Rab5a results in the mislocalization of rhoptry proteins and a subset of microneme proteins, to the dense granules, indicating a role in protein sorting (23). Another Rab GTPase, Rab6, is thought to localizes to both the Golgi and the dense granules although the function of Rab6 has not been defined (24). Syntaxin 6 (TgSyn6) marks yet another distinct PGC and appears to have a role in retrograde trafficking between the Rab5 and Rab7 compartments and the trans-golgi network (25). A fifth compartment, the plant-like vacuole (VAC) has similarities to the central vacuole in plants. This compartment contains lytic enzymes that are important for proteolytic processing of the micronemes, ion regulation and processing of endocytic material (26–28). Endocytosis has only recently been described in *T. gondii* (29,30). After uptake material is trafficked to the VAC (31,32). Although the function of PGCs have not been fully defined, these compartments mark a point of intersection between biosynthetic and endocytic pathways and are a hub for protein trafficking in the parasite.

The location of the PGCs adjacent to the apically positioned Golgi is presumed to optimize the transport of newly synthesized proteins to the parasite's apical end (22). However, the cytoskeletal factors which control endomembrane positioning have not been identified. In mammalian cells, vesicle transport and organelle positioning is controlled by the microtubule cytoskeleton and associated kinesin and dynein motors (33,34). In contrast, budding yeast uses bundled F-actin filaments as tracks for myosin V-based transport of vesicles, organelles and localizing RNA transcripts (35). *T. gondii* contains 22 highly-stable microtubules (MTs), that are strictly localized at the parasite pellicle (36–38) (Fig. 1a) and do not associate with organelles in the parasite cytosol. Moreover, microtubule depolymerization with oryzalin had no effect on dense granule transport (39) and thus are likely not involved in organelle positioning or vesicle transport between the post-Golgi compartments.

T. gondii has a single actin gene (TgAct1) that has 83% similarity with chicken skeletal actin (40). The organization of the actin cytoskeleton in *T. gondii* remained elusive for many years, most likely because of the low propensity TgAct1 to bind phalloidin, the gold standard reagent used to image actin in other cell types (41,42). This inability to visualize F-actin *in vivo*, in addition to biochemical studies which suggested that TgAct1 was incapable of forming long stable filaments *in vitro* led to the idea that short TgAct1 filaments formed only transiently during parasite motility and host cell invasion (reviewed by (43)). However, more recent studies have uncovered new biological roles for TgAct1 including apicoplast inheritance (a non-photosynthetic plastid organelle) (44), dense granule transport (39) and microneme recycling during parasite division (45). Additionally, an unconventional myosin motor, TgMyoF, was shown to be required for apicoplast inheritance and dense granule transport (39,44). With the development of a new reagent, the Actin chromobody™ (ActinCB) (46), actin filaments have now been visualized in both the parasite cytosol (46–48) and in a tubular network which connects individual parasites (46,49). These *in vivo* observations are consistent with recent *in vitro* experiments by Lu and colleagues who used a total internal reflectance (TIRF) microscopy-based approach to demonstrate that Pfact1, actin from the closely related apicomplexan parasite *Plasmodium falciparum,* is capable of transiently forming long filaments up to 30μm in length (50). Collectively, these findings have significantly altered our understandings of both the functions and organization of Apicomplexan actin.

The goal of this study was to investigate the role of actin and TgMyoF in regulating vesicle trafficking and organelle positioning within the endomembrane pathway. Our data demonstrates that both of these proteins are required for the apical positioning and morphology of the Golgi and post-Golgi compartments, ER tubule movement, and transport of Rab6-positive and Rop1-positive vesicles. These results indicate that this acto-myosin system is vital for controlling the organization of the endomembrane system in *T. gondii* and uncovers new biological roles of actin in the intracellular phase of the parasite's growth cycle.

126 # Results

127 ## Rab6 colocalizes with syntaxin6 in a post-Golgi compartment.

128 To investigate how the morphology and dynamics of the PGCs is controlled by the *T. gondii*
129 cytoskeleton, we fluorescently labeled the Rab5a and Rab6 PGCs by expressing
130 NeonGreenFP-Rab5a (referred to subsequently as Neon-Rab5a) and EmeraldFP-Rab6
131 (EmGFP-Rab6) along with Grasp55-mCherryFP, a marker of the cis-Golgi (23,24,51,52). As
132 expected, Neon-Rab5 did not co-localize with Grasp55-mCherryFP and was found in a distinct
133 compartment adjacent to the Golgi (23) (Fig.1B; upper panel). Surprisingly, Rab6 also did not
134 localize to the Golgi as previously reported (24) but also localized to a compartment apical to
135 the Golgi (Fig. 1B; lower panel). To determine if Rab6 colocalizes with markers of the other
136 post-Golgi compartments, we transfected parasites with AppleFP-Rab6 expression construct
137 along with Neon-Rab5, Neon-Rab7, Syn6-GFP, DrpB-GFP and SAG1ΔGPI-GFP, a marker for
138 the dense granules (23,31,53,54) and grew parasites for ~18 hours before fixation or live cell
139 imaging (Fig. 1C). Additionally, extracellular parasites expressing EmGFP-Rab6 were fixed and
140 stained with an anti-TgCPL antibody, a marker of the VAC (Fig. 1C) (27). Rab6 and Syn6
141 localize within the same post-Golgi compartment. Syn6 was also localized to the plasma
142 membrane but no peripheral staining of Rab6 was observed (Fig. 1C) (25). No colocalization
143 was observed between Rab6 and the other proteins analyzed (Fig. 1C) including the dense
144 granules which were previously reported to contain Rab6 on their surface (25) (Fig. 1C; panel
145 iv).

146 Live cell imaging of parasites expressing Syn6-GFP and AppleFP-Rab6 demonstrates
147 that these proteins occupy distinct sub-domains within the same tubular-vesicular compartment
148 (Fig. 2A and Fig. 2B; Video 1). Line scan analysis indicates that Syn6 and Rab6 are both found
149 in the "vesicular" domain of the compartment (Fig. 2B; magenta arrow) while Rab6
150 positive/Syn6 negative (Rab6(+)/Syn6(-)) tubules extend from this "vesicular" domain (Fig. 2B;
151 white bracket). Rab6(+) vesicles can be seen budding from the tip of the tubular extensions
152 (Fig. 2C). Rab6(+)/Syn6(-) vesicles are distributed throughout the parasite cytosol (Fig. 2D
153 arrowhead; video 1) and exhibited directed, presumably motor-driven, motion.

154 ## Rab6 vesicle transport is dependent on F-actin.

155 To further characterize the dynamics and morphology of the Rab6 compartment, we imaged
156 parasites expressing EmGFP-Rab6 using live cell microscopy with a temporal resolution of
157 100ms (Fig. 3A; Video 2). The Rab6 compartment is dynamic and undergoes constant
158 rearrangement as indicated by images taken after 5, 10 and 15 seconds of imaging (Fig. 3A,
159 middle panel; Video 2). Rab6(+) vesicles exhibited directed movement throughout the cytosol as
160 illustrated by kymographs (Fig. 3A, right panel). This motion was reminiscent of the directed
161 actin-based motion exhibited by dense granules (39). Tracking the movement of Rab6(+)
162 vesicles revealed velocities and run-lengths of 0.92±0.01μm/s and 1.6±0.03μm respectively
163 (Table S1).

164 Given the similarities between Rab6(+) vesicle movement and actin dependent dense granule
165 movement (39) we sought to determine if actin was required for Rab6(+) vesicle transport. We
166 treated intracellular parasites expressing EmGFP-Rab6 with cytochalasin D (CD) for 60 minutes
167 to depolymerize F-actin before commencement of imaging (Video 2). We observed two

168 phenotypes associated with the loss of F-actin: First, the main Rab6(+) compartment lost its
169 apical localization and became fragmented and distributed throughout the parasite cytosol (Fig.
170 3B). Second, the dynamic tubular morphology of the EmGFP-Rab6 compartment is lost and the
171 compartment remained static throughout the 60-second imaging period. Vesicle formation from
172 the Rab6 compartment was perturbed in CD treated parasites (Fig. 3B; right panel). The
173 number of Rab6(+) vesicles in the parasite cytosol decreases from an average of 8±0.5 in
174 control parasites (RH parasites treated with DMSO) to 3±0.3 after CD treatment (Fig. 3C).
175 Similarly, the number of directed runs exhibited by Rab6(+) vesicles decreased from 6±0.45 in
176 control to less than 1 after CD treatment (Fig. 3D).

177 Creation of conditional TgMyoF-knockdown parasite line.

178 Since dense granule transport is dependent on F-actin and TgMyoF (39), we investigated if
179 TgMyoF was also required for Rab6(+) vesicle transport or compartment dynamics. We
180 previously used an inducible Cre-LoxP system to create a parasite line deficient in functional
181 TgMyoF, however depletion of TgMyoF protein levels after TgMyoF gene excision took ~48
182 hours (39,55). Thus, we created an inducible TgMyoF knockdown (KD) parasite line using the
183 auxin-inducible degradation system where TgMyoF protein levels could be rapidly degraded
184 (56,57) (Fig. 4A). The endogenous TgMyoF gene was C-terminally tagged with an AID-HA
185 epitope to create a TgMyoF-mAID-HA parasite line (referred to subsequently as TgMyoF-AID).
186 PCR of genomic DNA and western blot was used to confirm the accurate integration of this
187 construct (Fig. 4B and Fig. S1). Treatment of TgMyoF-AID parasites with indole-3-acetic acid
188 (IAA) for four hours resulted in depletion of TgMyoF to undetectable levels (Fig. 4B). TgMyoF
189 depletion was independently confirmed by anti-HA immunofluorescence (IF) (Fig. 4C) and
190 TgMyoF-KD parasites exhibited aberrant apicoplast inheritance as demonstrated previously
191 (Fig. S1B) (39,44).

192 TgMyoF is required for apical positioning and structural integrity of
193 the PGCs

194 We were intrigued by the observation that F-actin was required for the apical positioning of the
195 Rab6 compartment. The post-golgi compartments have well-defined positions adjacent to the
196 Golgi, yet we have no mechanistic insight into how the position of these organelles is
197 maintained. To determine if TgMyoF is required for the apical positioning of the PGCs, we
198 ectopically expressed markers for these compartments, specifically EmGFP-Rab6, Neon-
199 Rab5a, Neon-Rab7, Syn6-GFP and DrpB-GFP in TgMyoF-AID parasites treated with ethanol
200 (EtOH; control) or IAA (to deplete TgMyoF) for 18 hours before fixation. As expected in control
201 parasites, these compartments were positioned at the apical end of the parasite (Fig. 5A left
202 panels). After TgMyoF depletion however, the Rab5a, Rab6, DrpB and Syn6 compartments
203 became fragmented and were found throughout the cytosol (Fig. 5A; right panels). For each
204 protein, we quantified the number of compartments per parasite and found a statistically
205 significant increase after TgMyoF depletion in each case (Fig. 5B). In the case of Rab7, this
206 protein had a diffuse localization in the cytosol after TgMyoF depletion (Fig. 5A). Since Rab6
207 and Syn6 are localized to the same compartment in control parasites, we sought to determine if
208 these proteins remained colocalized after compartment fragmentation. In TgMyoF deficient
209 parasites expressing AppleFP-Rab6 and Syn6-GFP, we found that the co-localization between

210 these proteins remained after compartment fragmentation (Fig. 5C). In addition, 70% of
211 parasites also contained Rab6+/Syn6- vesicles (Fig. 5C, lower panel, white arrows).

212 TgMyoF plays a role in Rab6 vesicle transport

213 To assess the role of TgMyoF in the Rab6 compartment and Rab6(+) vesicle dynamics,
214 TgMyoF-AID parasites expressing EmGFP-Rab6 were treated with either EtOH or IAA for 18
215 hours before live cell imaging. Similar to what was observed after actin depolymerization, loss of
216 TgMyoF resulted in fragmentation of the Rab6 compartment (Fig. 5A and 5B; left panels) and
217 loss of this compartments dynamic reorganization. (Fig. 6A and 6B middle panel). There was
218 also a decrease in the number of Rab6(+) vesicles exhibiting directed motion from 7.6±0.7 in the
219 control to 3±0.45 in TgMyoF-KD parasites (Fig. 6A and 6B right panels; Fig. 6C) (Video 3).
220 Although the number of directed runs was significantly reduced, vesicle velocities were the
221 same in the absence of TgMyoF compared with controls (Fig. 6D) (Table S1).

222 These data combined with published work demonstrate that TgMyoF and actin are required for
223 dense granule and Rab6+ vesicle transport (39), apical positioning of the post-golgi
224 compartments, and inheritance of the apicoplast (44). All of these organelles are part of the
225 endomembrane network in *T. gondii*. Therefore, we wanted to determine if other organelles in
226 this pathway, namely the ER, the Golgi, the micronemes and the rhoptries, relied on this acto-
227 myosin system for their dynamics and/or morphology.

228 TgMyoF-knockdown affects movement of ER tubules.

229 The ER is a large membrane bound organelle that has three distinct functional domains, the
230 nuclear envelope and peripheral tubules and peripheral cisternae which form an extensive
231 and continuous network in the parasite cytosol (52,58). Live cell imaging of parasites with a
232 fluorescently labeled ER, achieved by expression eGFP-SAG1ΔGPI-HDEL (53) (referred to
233 subsequently as GFP-HDEL) reveals that the ER tubules are highly dynamic and undergo
234 continuous reorganization (Video 4). ER tubule rearrangements are clearly evident when the
235 first frame of the movie was overlaid with images taken after 5, 10 and 15 seconds of imaging
236 (Fig 7A; right panel). ER tubule motility has been described previously in mammalian cells (59).
237 In this case, tubule dynamics are dependent on the microtubule cytoskeleton (60–62). To
238 determine if TgMyoF plays a role in ER dynamics in *T. gondii,* TgMyoF-AID parasites
239 expressing GFP-HDEL were imaged after TgMyoF depletion. Loss of TgMyoF did not result in
240 reorganization or collapse of the peripheral ER, however ER tubule motility is decreased as
241 illustrated with time overlay images (Fig. 7B; right panel) (Video 4).

242 Actin depolymerization and TgMyoF depletion results in Golgi
243 fragmentation.

244 Next, we investigated if loss of TgMyoF or actin depolymerization affected Golgi morphology.
245 The cis-golgi was fluorescently labeled by expressing Grasp55-mCherryFP in TgMyoF-AID
246 parasites. Parasites were treated in EtOH or IAA for 15 hours to deplete TgMyoF. In the
247 presence of TgMyoF, 80% of parasites contained a single Golgi localized at the apical end of
248 the nucleus while 20% of parasites were undergoing cell division and contain two Golgi per
249 parasite as expected (Fig. 8A, 8B & 8D). After TgMyoF knockdown, only 25% of parasites

250 contained a single Golgi, 52% contained two Golgi and 21% contained three Golgi (Fig. 8B and
251 8D). Similarly, actin depolymerization with cytochalasin D also resulted in an increased number
252 of Golgi per parasite (Fig. 8C and 8D). While the majority of Golgi remain closely associated
253 with the nucleus after TgMyoF-knockdown or CD treatment, the apical positioning of the Golgi
254 was lost. After TgMyoF depletion or actin depolymerization, 52% and 40% of parasites
255 respectively contained Golgi in both the apical and basal ends of the parasites compared to just
256 5% of control parasites (Fig 8E).

257 Since the Golgi in *T. gondii* divides by binary fission during cell division (51,63), the increased
258 number of Golgi observed after the loss of F-actin and TgMyoF could be due to uncoupling of
259 the Golgi division cycle from the cell cycle. To determine if this was the case, we first
260 determined the number of Golgi per parasite after 4 hours of IAA treatment, the time at which
261 TgMyoF is completely depleted and a length of time shorter than one parasite division cycle.
262 After 4 hours and 15 hours of IAA treatment, the number of Golgi per parasite is
263 indistinguishable indicating that Golgi fragmentation occurs quickly upon TgMyoF depletion but
264 does not continue to fragment with extended IAA treatment times (Fig 8D). Next, we
265 investigated if loss of TgMyoF affected the number of centrosomes per parasite as it had
266 previously been demonstrated that centrosome duplication and Golgi fission are the first events
267 to take place at the start of parasite division (52) (Fig. 8A). TgMyoF-AID parasites were
268 transfected with Grasp55-mCherry and centrin1-GFP (64) to label the Golgi and centrosomes
269 respectively, and then treated with EtOH or IAA for 15 hours. In control parasites, 73% of
270 parasites contained one Golgi and one centrin (1G/1C) while the remaining ~30% of parasites
271 were at various stages of division and contained either one Golgi and twp centrin (1G/2C) or two
272 Golgi and two centrin (2G/2C) (Fig. 7F and 7G). In contrast, only 20% of TgMyoF-KD parasites
273 contained one Golgi and one centrin (1G/1C), while 41% contained two Golgi and one centrin
274 (2G/1C), compared to just 3% of controls. 7% and 16% of IAA treated parasites contained one
275 centrin and three Golgi (1C/3G) or two centrin and three Golgi (2C/3G) respectively, which were
276 phenotypes that were never observed in the control parasites (Fig. 8F and 8G). The number of
277 centrosomes per parasite remained unchanged in TgMyoF-KD parasites compared to controls
278 (Fig. 8H). Thus, we conclude that TgMyoF and actin are important for controlling both Golgi
279 number and apical positioning and these effects on Golgi morphology are independent of the
280 parasite's cell division cycle.

281 TgMyoF depletion affects apical positioning of the rhoptries and Rop1 282 vesicle movement

283 It has been demonstrated previously that loss of TgMyoF results in accumulation of intact
284 micronemes and rhoptry proteins in the parasite's residual body (44). In our independently
285 generated TgMyoF conditional knockdown parasite line, we observe a similar phenotype. After
286 15 hours of IAA treatment, 73% of TgMyoF deficient vacuoles contained rhoptries (visualized by
287 expression of Rop1-NeonFP) in the residual body compared to just 14% of controls. While 67%
288 of TgMyoF deficient vacuoles exhibited accumulation of micronemes in the residual body
289 (visualized using an anti-AMA1 antibody) compared to 5% of controls (Fig. 9A and 9B). Despite
290 the accumulation of these organelles in the residual body, the apical positioning of the
291 micronemes was not affected in TgMyoF-knockdown parasites when assessed by IFA (Fig. 9A).
292 In contrast, there appeared to be an increased Rop1 fluorescence throughout the parasite
293 cytosol (Fig. 9A; magenta arrow). To further investigate the effects of TgMyoF depletion on

294 rhoptry dynamics, we expressed Rop1-NeonFP in TgMyoF-AID parasites treated for 18 hours
295 with either EtOH or IAA and imaged the parasites using live cell microscopy. In control
296 parasite's, the rhoptries were localized as expected at the apical end. The rhoptries were
297 surprisingly dynamic, and like the Rab6 compartment, were constantly rearranged (Fig. 9C,
298 inset; Video 5). In addition, Rop1 vesicles were observed throughout the parasite and exhibited
299 directed, motor-driven motion (Video 6). Upon TgMyoF knockdown we observed a large
300 decrease in the number of directed runs exhibited by Rop1-NeonFP vesicles from 11±1.1 in
301 control parasites to 1.4±0.2 after IAA treatment, even though the total number of Rop1 vesicles
302 was not statistically different between control and TgMyoF depleted parasites (6.25±0.4 and
303 9.1±0.6 in EtOH and IAA treated cells respectively) (Fig. 9E and 9F). To further investigate the
304 effect of TgMyoF knockdown on the apical positioning of the rhoptries, we compared Rop1-
305 NeonFP fluorescence intensity at the apical and basal ends in control and TgMyoF depleted
306 parasites. In control parasites the apical:basal ratio was 5.8±0.7, indicating a strong enrichment
307 of Rop1-NeonFP at the parasite's apical end. By comparison the apical:basal ratio in IAA
308 treated parasites was only 2.1±0.15. While Rop1 is still enriched at the parasites apical end,
309 there is an increase in Rop1-NeonFP fluorescence at the basal end of TgMyoF-KD parasites
310 compared to controls (Fig. 9G).

311 Discussion

312 The polarized endomembrane system in *T. gondii* is vitally important for the accurate trafficking
313 of secretory proteins to the micronemes, rhoptries and dense granules. Our data demonstrate
314 that F-actin and TgMyoF control the dynamics, positioning and morphology of the
315 endomembrane network in *T. gondii*.

316 Actin-driven ER tubule motility observed in *T. gondii* is reminiscent of the microtubule-controlled
317 ER tubule movements that have been described in mammalian cells (60,61,65) and
318 actin/myosin XI driven tubule movements in plants (66). The function of ER tubule movement is
319 best understood in mammalian cells, where ER tubules form contacts with numerous organelles
320 and regulates the timing and site of mitochondrial and endosome fission, as well as facilitating
321 lipid and calcium exchange between organelles (67–69). Future work is required to elucidate the
322 importance of ER tubule movement in *T. gondii* biology.

323 The Golgi in *T. gondii* is localized adjacent to the nuclear envelope at the parasite's apical end,
324 appearing as a single stack when imaged by conventional fluorescence microscopy. Early in the
325 parasite's cell division cycle, the Golgi elongates and divides by binary fission (52,63). A second
326 round of Golgi division then occurs, and two Golgi are inherited by each daughter (51) which
327 appear to coalesce to form a single Golgi stack. However, it remains undetermined whether the
328 two Golgi stacks undergo membrane fusion or if they are simply maintained in close proximity
329 such that the stacks cannot be resolved using diffraction-limited microscopy. In this study, we
330 quantified Golgi number four hours after TgMyoF depletion and one hour after actin
331 depolymerization with cytochalasin D. Golgi fragmentation had occurred at each of these time
332 points, with no accompanying effect on centrosome number suggesting the changes in Golgi
333 number are not due to a perturbation of the parasite's cell division cycle. One possible
334 explanation for these results could be that the Golgi may be comprised of a paired stack held
335 together in very close proximity in an actin-dependent manner. A similar observation was
336 recently made by Kondylis and colleagues who demonstrated in Drosophila S2 cells that the

337 Golgi consists of duplicated structural units that separated during the G2 phase of the cell cycle,
338 prior to mitosis (70). Golgi separation could be artificially induced upon actin depolymerization
339 with either cytochalasin D or latrunculin B (LatB). The observation that Golgi number did not
340 increase between the 4- and 15-hour IAA treatment times suggests that the number of structural
341 units that can be formed from a single Golgi is finite. In addition to the increase in Golgi
342 number, many Golgi failed to maintain their position at the parasite's apical end and were
343 observed associated with the lateral of basal sides of the nucleus (Fig. 8B and 8E). Collectively,
344 our data demonstrate that actin and TgMyoF control both Golgi number and positioning.

345 After exiting the Golgi, proteins destined for the micronemes and rhoptries are trafficked to one
346 or more post-Golgi compartments. We have identified Rab6 as a new marker of the syntaxin 6
347 compartment, a protein that plays a role in retrograde trafficking from the Rab5a/Rab7
348 compartments to the Golgi (25). Our data builds upon previously published results indicating
349 that Rab6 localizes to cytosolic vesicles and a compartment at the apical end of the nucleus,
350 thought previously to be the Golgi since TgRab6 localizes to the Golgi when heterologously
351 expressed in mammalian cells (25). However, we find no evidence that Rab6 is found in the cis-
352 or mid-Golgi. Additionally, while we also observe Rab6(+) vesicles throughout the parasite,
353 Rab6 does not colocalize with a marker for the dense granules, indicating these are distinct
354 vesicle types. This data is consistent with a recent report demonstrating that Rab11a is found on
355 the surface of dense granules and required for their secretion (71). The discrepancy between
356 our results and previously published data, is likely due to the unavailability of organelle markers
357 at the time of the previous publication (25).

358 The Rab6 compartments is dynamic and has tubular morphology that undergoes continuous
359 rearrangement, we observed new tubules growing from the compartment while others retract.
360 Vesicles were observed to bud from the tip of tubules and subsequently exhibited directed actin
361 and TgMyoF dependent movement. This dynamic morphology closely mirrors the dynamics of
362 endosomal compartments in mammalian cells. In this case, tubule formation is driven by the
363 coordinated activity of microtubule motors (72) and branched actin networks nucleated by
364 WASH and the Arp2/3 complex (73,74), along BAR domain-containing proteins that induce
365 membrane curvature (75). No recognizable BAR-domain containing proteins or Arp2/3 complex
366 proteins are found in *T. gondii,* (76,77) indicating that the molecular mechanisms underlying
367 tubule formation in the Rab6 compartment are distinct from the mechanisms of tubule formation
368 in mammalian cells and will require further investigation.

369 The apical localization of the Rab6/Syn6, Rab5a, Rab7 and DrpB compartments are all
370 dependent on F-actin and TgMyoF. This dependence on TgMyoF and actin for apical
371 positioning suggests that these post-Golgi compartments are associated with the actin
372 cytoskeleton, or that the physical connections between these compartments, that maintain the
373 compartments in close proximity at the apical end, are formed in an actin dependent manner.
374 Future studies are needed to further identify the molecular players that control the associations
375 between these compartments.

376 Formation of rhoptry organelles is cell cycle regulated and occurs in the mid to late stages of
377 daughter cell development (31,52). Upon exit from the Golgi, rhoptry proteins are trafficked
378 through the Rab5 compartment and then processed in a premature-rhoptry from which the
379 mature rhoptry develops (10,22). Rhoptries had previously been shown to accumulate in the
380 residual body upon actin depolymerization or TgMyoF knockdown, implicating TgMyoF in
381 rhoptry trafficking and/or apical anchoring. Here, we further characterized the role of TgMyoF in
382 rhoptry trafficking by imaging rhoptry dynamics in parasites expressing Rop1-NeonFP using
383 live cell microscopy. As observed with the Rab6 compartment, the rhoptries undergo continual

384 rearrangement and Rop1(+) vesicles were observed budding from the rhoptry bulb. Rop1
385 positive vesicles exhibited directed, TgMyoF-dependent movement throughout the parasite
386 cytosol. In the absence of TgMyoF, there was a significant decrease in the number of directed
387 runs exhibited by Rop1-NeonFP vesicles. Currently, we do not know the function or subcellular
388 destination of these rhoptry derived vesicles and further work will be required to elucidate their
389 biological role. These results suggest that although the rhoptries are formed once per cell cycle,
390 acto-myosin dependent trafficking of proteins to or from the rhoptries occurs continuously.

391 There is an incomplete understanding of the mechanisms by which the mature rhoptries
392 are anchored to the apical end of the parasite. In the absence of TgARO1, a membrane
393 associated rhoptry protein, the apical positioning of the rhoptries was lost completely (78). This
394 contrasts with the TgMyoF knockdown phenotypes where there is increased accumulation of
395 rhoptries throughout the parasite cytosol, shown by an increase in Rop1 fluorescence at the
396 parasite's basal end (Fig. 9G), even though most parasites retain at least some intact rhoptries
397 at the apical end. Thus, the TgARO1 knockdown parasites have a more severe rhoptry
398 localization defect than TgMyoF knockdown parasites. Although TgMyoF was shown to interact
399 indirectly with TgARO1 (78), the differences in the severity of these phenotypes suggest that
400 TgMyoF is not required for TgARO1 anchoring activity. Our data suggests that TgMyoF is
401 required for movement of immature rhoptries to the apical tip but is not required for TgARO1-
402 dependent anchoring once the organelles have reached their destination.

403 This study demonstrates that TgMyoF controls the dynamics, positioning, and movement of a
404 wide array of organelles in the endomembrane pathway in *T. gondii*. Future studies will be
405 important to elucidate the mechanism by which this single molecular motor controls the
406 movement of such a wide array of membranous cargos. Given the structural similarity between
407 TgMyoF and the well characterized cargo transporter myosin V, we previously hypothesized
408 that TgMyoF bound dense granules via its C-terminal WD40 domain and transported cargo by
409 moving processively on filamentous actin (39). The large number of membrane-bound
410 organelles whose movement is dependent on TgMyoF makes elucidating TgMyoFs mechanism
411 of action even more pertinent. Outstanding questions include: Does TgMyoF associate directly
412 with each membrane bound organelle? If so, what is the molecular basis of this association?
413 How do these molecular complexes vary for each cargo and how are these interactions
414 regulated? Does TgMyoF have the capacity to transport cargo as either a single motor or an
415 ensemble? Future work aimed at identifying TgMyoF interacting proteins and modes of
416 regulation will provide new insight into mechanisms of cargo transport in *T. gondii*.

417

418 # Materials and Methods

419 ## Cell culture and parasite transfection

420 *T. gondii* tachyzoites derived from RH strain were used in all experiments. Parasites were
421 maintained by continuous passage in human foreskin fibroblasts (HFFs) in Dulbecco's Modified
422 Eagle's Media (DMEM) (ThermoFisher, Carlsbad CA) containing 1% (v/v) heat inactivated fetal
423 bovine serum (FBS) (VWR, Radnor PA) , 1X antibiotic/antimycotic (ThermoFisher) as previously

424 described (79). Parasites were transfected as described previously (79) using a BTX
425 electroporator set as follow: voltage 1500V; resistance 25Ω and capacitance 25μF.

426 Drug treatment.

427 To determine the effect of actin depolymerization on endomembrane organization and
428 dynamics, transfected parasites were grown for 15-18 hours in confluent HFF monolayers,
429 treated for 60 minutes with either 2μM cytochalasin D or equivalent volume of DMSO before live
430 cell imaging as described below. To deplete TgMyoF, TgMyoF-AID parasites were treated with
431 a final concentration of 500μM IAA, diluted 1:1000 from a 500mM stock made in 100% EtOH.
432 For live cell imaging experiments treated time ranged from 15-18 hours. For western blot,
433 treatment time was varied as indicated in figure 3.

434 Construction of expression plasmids

435 A list of plasmids, primers and gene accession numbers used in this study can be found in
436 Tables S2, S3 and Table S5 respectively.

437 Creation of pTKOII-MyoF-mAID-HA:

438 pTKOII-MyoF-EmeraldGFP (EmGFP) (39) was digested with BglII and AflII to remove the
439 EmGFP coding sequence. AID-HA was amplified by PCR using the AID-HA ultramer as a
440 template and primer pairs AID-HA F and AID-HA R. Plasmid backbone and the PCR product
441 was gel purified and ligated via Gibson assembly using NEBuilder HiFi DNA assembly master
442 mix as per manufacturer's instructions (New England BioLabs; Ipswich, MA). Plasmids were
443 transfected into NEB5α bacteria and positive clones screened by PCR and verified by Sanger
444 sequencing.

445 Creation of pmin-eGFP-Rab6-Ble:

446 To create parental plasmid pmin-eGFP-mCherry-Ble, pmin-eGFP-mCherry was digested with
447 KpnI and XbaI. pGra1-Ble-SAG1-3'UTR plasmid (80) was digested with KpnI and XhoI to
448 remove the ble expression cassette. A fill-in reaction was performed to produce blunt ends by
449 incubating plasmids with 100μM dNTPs and T4 DNA polymerase at 12°C for 15 minutes.
450 Digested plasmids were gel purified and ligated together using T4 DNA ligase (New England
451 Biolabs). Plasmids were transfected into NEB5α bacteria and positive clones screened by PCR
452 and verified by Sanger sequencing. To create pmin-EmGFP-Rab6-ble, pmin-eGFP-mCherry-Ble
453 was digested with NheI and AflII to remove eGFP-mCherry sequence. EmGFP was amplified by
454 PCR with EmGFP-R6F and EmGFP-R6R primer pairs using pTKOII-MyoF-EmGFP as a
455 template. Rab6 coding sequence was amplified by PCR using RH cDNA as a template and
456 Rab6F and Rab6R primers. Digested plasmid backbone, EmGFP and Rab6 PCR products were
457 gel purified and ligated using NEBuilder HiFi DNA assembly master mix as per manufacturer's
458 instructions (New England BioLabs). Plasmids were transfected into NEB5α bacteria and
459 positive clones screened by PCR and verified by Sanger sequencing.

460 Creation of ptub-SAG1-ΔGPI-HDEL:

461 Parental plasmid ptub-SAG1-ΔGPI (39) was digested with AflII. HDEL ultramers (Table S3)
462 reconstituted to a concentration of 200mM in duplex buffer (100mM K Acetate; 30mM Hepes pH

463 7.5), were combined in equal ratios and headed to 95°C for 5 minutes before cooling slowly to
464 room temperature. Duplexed ultramers were diluted 1:100 in molecular biology grade water and
465 ligated to digested plasmid using NEBuilder HiFi DNA assembly master mix as per
466 manufacturer's instructions (New England BioLabs). Plasmids were transfected into NEB5α
467 bacteria and verified by Sanger sequencing.

468 **Creation of pmin-NeonFP-Rab5a and pmin-NeonFP-Rab7.**

469 Rab5a and Rab7 coding sequences were amplified by PCR using primers sets Rab5F/R,
470 Rab7F/R and pTg-HARab5a and pTg-HARab7 (27,81) as templates. NeonGreen was amplified
471 by PCR using Neon-R5F/Neon-R5R, Neon-R7F/Neon-R7R primer sets and Ty1-
472 NeonGreenPave as a template. pmin-EmGFP-Rab6 plasmid was digested with NheI and AflII
473 to remove EmGfP-Rab6 coding sequence. Plasmid backbones and PCR products were gel
474 purified and annealed using Gibson assembly with NEBuilder HiFi DNA assembly master mix as
475 per manufacturer's instructions. Plasmids were transfected into NEB5α bacteria and positive
476 clones screened by colony PCR and verified by Sanger sequencing.

477 **Creation of ptub-Rop1-NeonGreenFP.**

478 ptub-SAG1-ΔGPI-GFP plasmid was digested with NheI and AflII to remove SAG1-GFP coding
479 sequence. Rop1-GFP coding sequence was amplified using Rop1 F/R primer pairs and RH
480 cDNA as a template. NeonGreen was amplified by PCR using NeonRop1F and NeonRop1R
481 primer pairs. Plasmid backbones and PCR products were gel purified and annealed using
482 Gibson assembly with NEBuilder HiFi DNA assembly master mix as per manufacturer's
483 instructions. Plasmids were transfected into NEB5α bacteria and positive clones screened by
484 PCR and verified by Sanger sequencing.

485 Creation of TgMyoF-AID parasite line.

486 The *pTKO2_MyoF_mAID-HA* plasmid was linearized with SphI and 25μg was transfected into
487 $1x10^7$ *ΔKu80:ΔHXGPRT:Flag-Tir1* parental parasites (a gift from Dr. David Sibley, Washington
488 University (56)). Parasites were selected using mycophenolic acid (MPA) (25 μg/ml) and
489 xanthine (50 μg/ml) until approximately 70% of the parasites were HA positive. Clonal parasite
490 lines were obtained by limited dilution into a 96 well plate. After 7 days of growth, wells
491 containing a single plaque were selected for further analysis. All HA positive clones were
492 amplified in a 6 well plate and genomic DNA isolated using Qiagen DNAeasy blood and tissue
493 kit as per manufactures instructions (Qiagen, Germantown, MD) (Cat #69504). Genomic DNA
494 was analyzed for correct insertion of the pTKO2_MyoF_mAID HA plasmid into the TgMyoF
495 genomic locus by PCR using primers listed in Table S3 as outlined in Fig. S1.

496 Western blot

497 To assess the extent of TgMyoF depletion after auxin addition as a function of time, $8x10^6$
498 extracellular TgMyoF-AID parasites were incubated in 500μl of DMEM containing 1% FBS,
499 antibiotic/antimycotic and 500μM IAA and incubated at 37°C, 5% CO_2 for 0, 0.5, 1, 2, or 4 hours.
500 At each time point parasites were centrifuged at 1200xg for 5 minutes and resuspend in 25ul of
501 1xPBS containing protease inhibitor cocktail (MilliporeSigma, St. Louis MO; Cat # P8340). 25ul
502 of 2XLamelli buffer (Biorad, Hercules, CA; Cat # 1610737) containing 100mM DTT was added

503 to each sample and boiled at 95°C for 10 minutes. Samples were run on 4-12% gradient gel
504 (Biorad; Cat# 456-1064), transferred to PVDF for 60 minutes at 4°C at 100V using the Biorad
505 blotting system. PVDF membranes were blocked overnight at 4°C in 5% milk, 1XTBS-T (150mM
506 NaCl, 20mM Tris base, 0.1% tween20 (v/v) pH 7.4) before blotting with tubulin and HA primary
507 antibodies and anti-mouse and anti-rat secondary antibodies. All antibodies were incubated with
508 PVDF for 60 minutes at room temperature with 3x10-minute washes with 1xTBS-T in between
509 antibody incubations. Immunoblots were developed using Pierce ECL western blotting substrate
510 (ThermoFisher, Cat# 32209) and visualized using LiCor Odyssey Fc. Antibody dilutions and
511 product information can be found in Table S4.

512 Microscopy

513 Parasite transfection for live cell imaging or immunocytochemistry.

514 25µg of each plasmid was transfected as described above. Transfected parasites were grown
515 for 15-18 hours in confluent HFF monolayers grown on either MatTek dishes (MatTek
516 corporation, Ashland MA) or on coverslips before either live cell imaging or
517 immunocytochemistry.

518 Live cell microscopy.

519 Growth media was replaced with Fluorobrite DMEM (ThermoFisher; Cat# A19867) containing
520 1% FBS and 1x antimycotic/antibiotic pre-warmed to 37˚C. Images were acquired on a GE
521 Healthcare DeltaVision Elite microscope system built on an Olympus base with a 100x 1.39 NA
522 objective in an environmental chamber heated to 37˚C. This system is equipped with a scientific
523 CMOS camera and DV Insight solid state illumination module. Image acquisition speeds were
524 determined on a case-by-case basis as noted in the video legends.

525 Immunocytochemistry.

526 Parasites were fixed with freshly made 4% paraformaldehyde (Electron microscopy sciences,
527 Hatfield, PA; Cat# 15714) in 1xPBS (ThermoFisher; Cat# 18912-014) for 15 minutes at RT.
528 Cells were washed three times in 1xPBS and permeabilized in 0.25% TX-100 diluted in 1xPBS
529 for 10 minutes at room temperature before washing three times in 1xPBS. Cells were blocked in
530 2% BSA-1XPBS for 15 minutes before antibody incubations. All antibodies were diluted in 0.5%
531 BSA-1xPBS at the concentrations indicated in Table S4. DNA was stained with 10µM DAPI
532 diluted in 1xPBS for 10 minutes and then washed three times in 1xPBS. Cells in mattek dishes
533 were either imaged immediately or stored in 1xPBS at 4˚C. Coverslips were mounted onto
534 slides using Prolong Gold anti-fade reagent (ThermoFisher; Cat # P36930) and allowed to dry
535 overnight before imaging.

536 Image analysis

537 Vesicle tracking and counting.

538 Vesicle tracking was performed using MtrackJ plug-in in Fiji (National Institutes of Health) as
539 previously described (82). Line scan analysis was performed using the “plot profile” tool in Fiji.
540 Kymographs were made using Fiji plugin KymographBuilder. Fiji plugin cell counter was used to

541 quantify the number of vesicles/parasites. Statistical significance was determined using students
542 t-test.

543 **Effect of TgMyoF depletion on post-Golgi compartment number.**

544 To count number of PGC "objects" in each parasite in control and TgMyoF knockdown
545 parasites, transfected parasites were fixed and stained with the anti-IMC1 antibody and DAPI
546 and z-stack images were acquired using Deltavision elite imaging system. For each PGC
547 image, maximum intensity projection of Z-stacked images were converted to binary images
548 using Fiji and particles counted using the "analyze particles" tool. IMC1 staining was used to
549 determine number of parasites/vacuole. Statistical significance was determined using students
550 t-test.

551 **Quantification of Golgi and centrosome number.**

552 To quantify the number of Golgi and centrosome per parasite, TgMyoF-AID parasites were
553 transfected with Grasp55-GFP plasmid alone or Grasp55-mCherry and Centrin1-GFP plasmids,
554 grown in confluent HFF monolayers overnight and treated with either EtOH or IAA for the final 4-
555 or 15- hours of growth before fixation and processing for immunofluorescence. Number of Golgi
556 per parasite and number of centrosomes per parasites were counted manually using the cell
557 count tool in Fiji. Statistical significance was determined using students t-test.

558 **Quantification of rhoptry and micronemes in the residual body.**

559 To quantify the number of parasites with microneme and rhoptry proteins in the residual body,
560 TgMyoF parasites were transfected with Rop1-NeonFP plasmid, and were grown for 15 hours in
561 either EtOH or IAA before fixation and immunocytochemistry with an anti-AMA1 antibody (Table
562 S4). The number of vacuoles containing rhoptries or micronemes in the residual body were
563 manually counted. N = 57 vacuoles for AMA-1 quantitation, N=77 vacuoles for Rop-1
564 quantitation from two independent experiments. Statistical significance was determined using
565 students t-test.

566 **Loss of rhoptry positioning at the parasites' apical end.**

567 To quantify Rop1 localization at the apical or basal ends of the parasite, Rop1-NeonFP was
568 transiently expressed in TgMyoF-AID parasites treated with EtOH or IAA for 15 hours. Parasites
569 were imaged live as described above. Using the first frame of each movie, the apical half and
570 the basal half of each parasite was outlined manually and the mean fluorescent intensity of
571 Rop1 in the apical and basal ends of the parasites were calculated using Fiji. The apical to
572 basal mean fluorescence intensity was calculated for each parasite. A ratio of 1 indicates that
573 Rop1 is evenly distributed in the apical and basal ends. A ratio >1 indicates more rop1 is
574 localized in the apical end than the basal end and a ratio <1 indicates more rop1 in the basal
575 end compared to the apical end. Rop1-NeonFP fluorescence in the residual body was excluded
576 from this analysis. Statistical significance was determined using students t-test.

577 **Statistics.**

578 Statistical analyses were performed using GraphPad Prism. Superplots were made as
579 described in (83).

Funding Information:

This work was funded by National Institutes of Health R21AI121885 awarded to ATH and the University of Connecticut Research excellence program awarded to ATH. The funders had no role in study design, data collection and interpretation, the decision to submit the work for publication or manuscript preparation. The authors declare that no competing interests exist.

Acknowledgements.

We thank members of the Heaslip Lab, Dr. Ken Campellone and members of the Campellone lab (University of Connecticut) for helpful discussion during the course of these experiments. We thank our colleagues for sharing reagents: Dr. Gary Ward (University of Vermont) for the IMC-1 and AMA-1 antibodies; Dr. Markus Meissner (Ludwig-Maximilian University, Munich) for the DrpB and Syntaxin 6 expression constructs; Dr. Vern Carruthers (University of Michigan) for the TgCPL antibody and the Rab5 an Rab7 expression plasmids. Dr. David Sibley (Washington University, St. Louis) for sharing the Flag-Tir1 parasite line; Dr. Boris Striepen (University of Pennsylvania) for the anti-Cpn60 antibody.

References.

1. Levine ND. The Taxonomy of Sarcocystis (Protozoa, Apicomplexa) Species. J Parasitol. 1986;

2. Levine ND. The protozoan phylum apicomplexa. The Protozoan Phylum Apicomplexa. 2018.

3. Rorman E, Zamir CS, Rilkis I, Ben-David H. Congenital toxoplasmosis-prenatal aspects of Toxoplasma gondii infection. Vol. 21, Reproductive Toxicology. Reprod Toxicol; 2006. p. 458–72.

4. Wang ZD, Wang SC, Liu HH, Ma HY, Li ZY, Wei F, et al. Prevalence and burden of Toxoplasma gondii infection in HIV-infected people: a systematic review and meta-analysis. Lancet HIV. 2017 Apr 1;4(4):e177–88.

5. Torgerson PR, Mastroiacovo P. The global burden of congenital toxoplasmosis: a systematic review. Bull World Heal Organ. 2013 Jul;91(7):501–8.

6. Pappas G, Roussos N, Falagas ME. Toxoplasmosis snapshots: Global status of Toxoplasma gondii seroprevalence and implications for pregnancy and congenital toxoplasmosis. Int J Parasitol [Internet]. 2009;39(12):1385–94. Available from: http://dx.doi.org/10.1016/j.ijpara.2009.04.003

7. Blader IJ, Coleman BI, Chen C-T, Gubbels M-J. Lytic Cycle of Toxoplasma gondii : 15

615 Years Later . Annu Rev Microbiol. 2015;69(1):463–85.

616 8. Dubois DJ, Soldati-Favre D. Biogenesis and secretion of micronemes in Toxoplasma
617 gondii. Vol. 21, Cellular Microbiology. Blackwell Publishing Ltd; 2019.

618 9. Carruthers VB, Tomley FM. Microneme proteins in apicomplexans. Subcell Biochem
619 [Internet]. 2008;47:33–45. Available from: http://www.ncbi.nlm.nih.gov/pubmed/18512339

620 10. Dubremetz JF. Rhoptries are major players in {Toxoplasma} gondii invasion and host cell
621 interaction. Cell Microbiol [Internet]. 2007 Apr [cited 2011 Dec 10];9(4):841–8. Available
622 from: http://www.ncbi.nlm.nih.gov/pubmed/17346309

623 11. Besteiro S, Dubremetz JF, Lebrun M. The moving junction of apicomplexan parasites: A
624 key structure for invasion. Cell Microbiol. 2011 Jun;13(6):797–805.

625 12. Besteiro S, Michelin A, Poncet J, Dubremetz JF, Lebrun M. Export of a Toxoplasma
626 gondii rhoptry neck protein complex at the host cell membrane to form the moving
627 junction during invasion. PLoS Pathog. 2009;

628 13. Beck JR, Chen AL, Kim EW, Bradley PJ. RON5 Is Critical for Organization and Function
629 of the Toxoplasma Moving Junction Complex. PLoS Pathog. 2014;

630 14. Alexander DL, Mital J, Ward GE, Bradley P, Boothroyd JC. Identification of the moving
631 junction complex of Toxoplasma gondii: A collaboration between distinct secretory
632 organelles. PLoS Pathog. 2005;1(2):0137–49.

633 15. Lebrun M, Michelin A, El Hajj H, Poncet J, Bradley PJ, Vial H, et al. The rhoptry neck
634 protein RON4 relocalizes at the moving junction during Toxoplasma gondii invasion. Cell
635 Microbiol. 2005;

636 16. Bougdour A, Tardieux I, Hakimi MA. Toxoplasma exports dense granule proteins beyond
637 the vacuole to the host cell nucleus and rewires the host genome expression. Cell
638 Microbiol [Internet]. 2014;16(3):334–43. Available from:
639 http://www.ncbi.nlm.nih.gov/pubmed/24373221

640 17. Bougdour A, Durandau E, Brenier-Pinchart MP, Ortet P, Barakat M, Kieffer S, et al. Host
641 cell subversion by Toxoplasma GRA16, an exported dense granule protein that targets
642 the host cell nucleus and alters gene expression. Cell Host Microbe. 2013;13(4):489–500.

643 18. Mercier C, Adjogble KD, Daubener W, Delauw MF. Dense granules: are they key
644 organelles to help understand the parasitophorous vacuole of all apicomplexa parasites?
645 Int J Parasitol [Internet]. 2005;35(8):829–49. Available from:
646 http://www.ncbi.nlm.nih.gov/pubmed/15978597

647 19. Karsten V, Qi H, Beckers CJM, Reddy A, Dubremetz JF, Webster P, et al. The protozoan
648 parasite Toxoplasma gondii targets proteins to dense granules and the vacuolar space
649 using both conserved and unusual mechanisms. J Cell Biol. 1998;

650 20. Chaturvedi S, Qi H, Coleman D, Rodriguez A, Hanson PI, Striepen B, et al. Constitutive
651 calcium-independent release of Toxoplasma gondii dense granules occurs through the
652 NSF/SNAP/SNARE/Rab machinery. J Biol Chem [Internet]. 1999;274(4):2424–31.
653 Available from: http://www.ncbi.nlm.nih.gov/pubmed/9891012

654 21. Zeigerer A, Gilleron J, Bogorad RL, Marsico G, Nonaka H, Seifert S, et al. Rab5 is
655 necessary for the biogenesis of the endolysosomal system in vivo. Nature. 2012 May
656 24;485(7399):465–70.

657 22. Venugopal K, Marion S. Secretory organelle trafficking in Toxoplasma gondii: A long story
658 for a short travel. Int J Med Microbiol. 2018;308(7):751–60.

659 23. Kremer K, Kamin D, Rittweger E, Wilkes J, Flammer H, Mahler S, et al. An
660 Overexpression Screen of Toxoplasma gondii Rab-GTPases Reveals Distinct Transport
661 Routes to the Micronemes. PLoS Pathog. 2013;9(3).

662 24. Stedman TT, Sussmann AR, Joiner KA. Toxoplasma gondii Rab6 mediates a retrograde
663 pathway for sorting of constitutively secreted proteins to the Golgi complex. J Biol Chem.
664 2003 Feb 14;278(7):5433–43.

665 25. Jackson AJ, Clucas C, Mamczur NJ, Ferguson DJ, Meissner M. Toxoplasma gondii
666 Syntaxin 6 Is Required for Vesicular Transport Between Endosomal-Like Compartments
667 and the Golgi Complex. Traffic. 2013;14(11):1166–81.

668 26. Miranda K, Pace DA, Cintron R, Rodrigues JCF, Fang J, Smith A, et al. Characterization
669 of a novel organelle in Toxoplasma gondii with similar composition and function to the
670 plant vacuole. Mol Microbiol. 2010;76(6):1358–75.

671 27. Parussini F, Coppens I, Shah PP, Diamond SL, Carruthers VB. Cathepsin L occupies a
672 vacuolar compartment and is a protein maturase within the endo/exocytic system of
673 Toxoplasma gondii. Mol Microbiol. 2010;76(6):1340–57.

674 28. Stasic AJ, Chasen NM, Dykes EJ, Vella SA, Asady B, Starai VJ, et al. The Toxoplasma
675 Vacuolar H+-ATPase Regulates Intracellular pH and Impacts the Maturation of Essential
676 Secretory Proteins. Cell Rep. 2019 May 14;27(7):2132-2146.e7.

677 29. Gras S, Jimenez-Ruiz E, Klinger CM, Schneider K, Klingl A, Lemgruber L, et al. An
678 endocytic-secretory cycle participates in Toxoplasma gondii in motility. PLoS Biol. 2019
679 Jun 1;17(6).

680 30. Dou Z, McGovern OL, Di Cristina M, Carruthers VB. Toxoplasma gondii ingests and
681 digests host Cytosolic proteins. MBio. 2014 Jul 15;5(4).

682 31. McGovern OL, Rivera-Cuevas Y, Kannan G, Narwold AJ, Carruthers VB. Intersection of
683 endocytic and exocytic systems in Toxoplasma gondii. Traffic. 2018 May 1;19(5):336–53.

684 32. Spielmann T, Gras S, Sabitzki R, Meissner M. Endocytosis in Plasmodium and
685 Toxoplasma Parasites. Trends in Parasitology. 2020.

686 33. Hirokawa N, Noda Y, Tanaka Y, Niwa S. Kinesin superfamily motor proteins and
687 intracellular transport. Nat Rev Mol Cell Biol [Internet]. 2009;10(10):682–96. Available
688 from: http://dx.doi.org/10.1038/nrm2774

689 34. Reck-Peterson SL, Redwine WB, Vale RD, Carter AP. The cytoplasmic dynein transport
690 machinery and its many cargoes. Nature Reviews Molecular Cell Biology. 2018.

691 35. Hammer JA, Sellers JR. Walking to work: Roles for class v myosins as cargo
692 transporters. Nat Rev Mol Cell Biol [Internet]. 2012;13(1):13–26. Available from:
693 http://dx.doi.org/10.1038/nrm3248

694 36. Morrissette NS, Sibley LD. Disruption of microtubules uncouples budding and nuclear
695 division in Toxoplasma gondii. J Cell Sci [Internet]. 2002;115(Pt 5):1017–25. Available
696 from: http://www.ncbi.nlm.nih.gov/pubmed/11870220

697 37. Morrissette NS, Sibley LD. Cytoskeleton of apicomplexan parasites. Microbiol Mol Biol

698 Rev [Internet]. 2002;66(1):21–38; table of contents. Available from:
699 http://www.ncbi.nlm.nih.gov/pubmed/11875126

700 38. NICHOLS BA, CHIAPPINO ML. Cytoskeleton of Toxoplasma gondii. J Protozool.
701 1987;34(2):217–26.

702 39. Heaslip AT, Nelson SR, Warshaw DM. Dense granule trafficking in Toxoplasma gondii
703 requires a unique class 27 myosin and actin filaments. Mol Biol Cell [Internet].
704 2016;27(13):2080–9. Available from: http://www.molbiolcell.org/cgi/doi/10.1091/mbc.E15-
705 12-0824

706 40. Dobrowolski JM, Niesman IR, Sibley LD. Actin in the parasite Toxoplasma gondii is
707 encoded by a single copy gene, ACT1 and exists primarily in a globular form. Cell Motil
708 Cytoskelet [Internet]. 1997/01/01. 1997;37(3):253–62. Available from:
709 http://www.ncbi.nlm.nih.gov/pubmed/9227855

710 41. Skillman KM, Diraviyam K, Khan A, Tang K, Sept D, Sibley LD. Evolutionarily divergent,
711 unstable filamentous actin is essential for gliding motility in apicomplexan parasites. PLoS
712 Pathog [Internet]. 2011/10/15. 2011;7(10):e1002280. Available from:
713 http://www.ncbi.nlm.nih.gov/pubmed/21998582

714 42. Schuler H, Matuschewski K. Regulation of apicomplexan microfilament dynamics by a
715 minimal set of actin-binding proteins. Traffic [Internet]. 2006;7(11):1433–9. Available
716 from: http://www.ncbi.nlm.nih.gov/pubmed/17010119

717 43. Sibley LD. Intracellular Parasite Invasion Strategies [Internet]. Vol. 304, Science.
718 Science; 2004 [cited 2020 Jun 23]. p. 248–53. Available from:
719 https://pubmed.ncbi.nlm.nih.gov/15073368/

720 44. Jacot D, Daher W, Soldati-Favre D. Toxoplasma gondii myosin F, an essential motor for
721 centrosomes positioning and apicoplast inheritance. EMBO J [Internet]. 2013/05/23.
722 2013; Available from: http://www.ncbi.nlm.nih.gov/pubmed/23695356

723 45. Periz J, Del Rosario M, McStea A, Gras S, Loney C, Wang L, et al. A highly dynamic F-
724 actin network regulates transport and recycling of micronemes in Toxoplasma gondii
725 vacuoles. Nat Commun. 2019 Dec 1;10(1).

726 46. Periz J, Whitelaw J, Harding C, Gras S, Minina MIDR, Latorre-Barragan F, et al.
727 Toxoplasma gondii F-actin forms an extensive filamentous network required for material
728 exchange and parasite maturation. Elife. 2017;6:1–29.

729 47. Stortz JF, Del Rosario M, Singer M, Wilkes JM, Meissner M, Das S. Formin-2 drives
730 polymerisation of actin filaments enabling segregation of apicoplasts and cytokinesis in
731 Plasmodium falciparum. Elife. 2019;

732 48. Tosetti N, Pacheco NDS, Favre DS, Jacot D. Three f-actin assembly centers regulate
733 organelle inheritance, cell-cell communication and motility in toxoplasma gondii. Elife.
734 2019;

735 49. Hunt A, Russell MRG, Wagener J, Kent R, Carmeille R, Peddie CJ, et al. Differential
736 requirements for cyclase-associated protein (CAP) in actin-dependent processes of
737 toxoplasma gondii. Elife. 2019;

738 50. Lu H, Fagnant PM, Trybus KM. Unusual dynamics of the divergent malaria parasite
739 PfAct1 actin filament. Proc Natl Acad Sci U S A. 2019;116(41):20418–27.

740 51. Pelletier L, Stern CA, Pypaert M, Sheff D, Ngô HM, Roper N, et al. Golgi biogenesis in
741 Toxoplasma gondii. Nature. 2002 Aug 1;418(6897):548–52.

742 52. Nishi M, Hu K, Murray JM, Roos DS. Organellar dynamics during the cell cycle of
743 Toxoplasma gondii. J Cell Sci [Internet]. 2008;121(9):1559–68. Available from:
744 http://jcs.biologists.org/cgi/doi/10.1242/jcs.021089

745 53. Striepen B, Soldati D, Garcia-Reguet N, Dubremetz JF, Roos DS. Targeting of soluble
746 proteins to the rhoptries and micronemes in Toxoplasma gondii. Mol Biochem Parasitol.
747 2001;113(1):45–53.

748 54. Breinich MS, Ferguson DJ, Foth BJ, van Dooren GG, Lebrun M, Quon D V, et al. A
749 dynamin is required for the biogenesis of secretory organelles in Toxoplasma gondii. Curr
750 Biol [Internet]. 2009;19(4):277–86. Available from:
751 https://www.ncbi.nlm.nih.gov/pubmed/19217293

752 55. Andenmatten N, Egarter S, Jackson AJ, Jullien N, Herman JP, Meissner M. Conditional
753 genome engineering in Toxoplasma gondii uncovers alternative invasion mechanisms.
754 Nat Methods [Internet]. 2012/12/25. 2013;10(2):125–7. Available from:
755 http://www.ncbi.nlm.nih.gov/entrez/query.fcgi?cmd=Retrieve&db=PubMed&dopt=Citation
756 &list_uids=23263690

757 56. Brown KM, Long S, Sibley LD. Plasma membrane association by N-acylation governs
758 PKG function in Toxoplasma gondii. MBio. 2017;8(3):1–14.

759 57. Brown K, Long S, Sibley L. Conditional Knockdown of Proteins Using Auxin-inducible
760 Degron (AID) Fusions in Toxoplasma gondii. BIO-PROTOCOL. 2018;

761 58. Lee CA, Blackstone C. ER morphology and endo-lysosomal crosstalk: Functions and
762 disease implications. Biochimica et Biophysica Acta - Molecular and Cell Biology of
763 Lipids. 2020.

764 59. Friedman JR, Voeltz GK. The ER in 3D: A multifunctional dynamic membrane network.
765 Vol. 21, Trends in Cell Biology. Trends Cell Biol; 2011. p. 709–17.

766 60. Woźniak MJ, Bola B, Brownhill K, Yang YC, Levakova V, Allan VJ. Role of kinesin-1 and
767 cytoplasmic dynein in endoplasmic reticulum movement in VERO cells. J Cell Sci. 2009
768 Jun 15;122(12):1979–89.

769 61. Friedman JR, Webster BM, Mastronarde DN, Verhey KJ, Voeltz GK. ER sliding dynamics
770 and ER-mitochondrial contacts occur on acetylated microtubules. J Cell Biol. 2010 Aug
771 9;190(3):363–75.

772 62. Grigoriev I, Gouveia SM, van der Vaart B, Demmers J, Smyth JT, Honnappa S, et al.
773 STIM1 Is a MT-Plus-End-Tracking Protein Involved in Remodeling of the ER. Curr Biol.
774 2008 Feb 12;18(3):177–82.

775 63. Hartmann J, Hu K, He CY, Pelletier L, Roos DS, Warren G. Golgi and centrosome cycles
776 in Toxoplasma gondii. Mol Biochem Parasitol. 2006 Jan;145(1):125–7.

777 64. Hu K. Organizational changes of the daughter basal complex during the parasite
778 replication of Toxoplasma gondii. PLoS Pathog. 2008;4(1):0108–21.

779 65. Waterman-Storer CM, Salmon ED. Endoplasmic reticulum membrane tubules are
780 distributed by microtubules in living cells using three distinct mechanisms. Curr Biol. 1998
781 Jul 2;8(14):798–807.

782 66. Griffing LR, Gao HT, Sparkes I. ER network dynamics are differentially controlled by
783 myosins XI-K, XI-C, XI-E, XI-I, XI-1, and XI-2. Front Plant Sci. 2014;

784 67. Phillips MJ, Voeltz GK. Structure and function of ER membrane contact sites with other
785 organelles. Vol. 17, Nature Reviews Molecular Cell Biology. Nature Publishing Group;
786 2016. p. 69–82.

787 68. Friedman JR, Lackner LL, West M, DiBenedetto JR, Nunnari J, Voeltz GK. ER tubules
788 mark sites of mitochondrial division. Science (80-). 2011 Oct 21;334(6054):358–62.

789 69. Hoyer MJ, Chitwood PJ, Ebmeier CC, Striepen JF, Qi RZ, Old WM, et al. A Novel Class
790 of ER Membrane Proteins Regulates ER-Associated Endosome Fission. Cell. 2018;

791 70. Kondylis V, van Nispen tot Pannerden HE, Herpers B, Friggi-Grelin F, Rabouille C. The
792 Golgi Comprises a Paired Stack that Is Separated at G2 by Modulation of the Actin
793 Cytoskeleton through Abi and Scar/WAVE. Dev Cell. 2007 Jun 5;12(6):901–15.

794 71. Venugopal K, Chehade S, Werkmeister E, Barois N, Periz J, Lafont F, et al. Rab11A
795 regulates dense granule transport and secretion during Toxoplasma gondii invasion of
796 host cells and parasite replication. PLoS Pathog. 2020;

797 72. Gautreau A, Oguievetskaia K, Ungermann C. Function and regulation of the endosomal
798 fusion and fission machineries. Cold Spring Harb Perspect Biol. 2014 Mar;6(3).

799 73. Derivery E, Sousa C, Gautier JJ, Lombard B, Loew D, Gautreau A. The Arp2/3 Activator
800 WASH Controls the Fission of Endosomes through a Large Multiprotein Complex. Dev
801 Cell. 2009 Nov 17;17(5):712–23.

802 74. Gomez TS, Billadeau DD. A FAM21-Containing WASH Complex Regulates Retromer-
803 Dependent Sorting. Dev Cell. 2009 Nov 17;17(5):699–711.

804 75. Frost A, Unger VM, De Camilli P. The BAR Domain Superfamily: Membrane-Molding
805 Macromolecules. Vol. 137, Cell. Cell; 2009. p. 191–6.

806 76. Baum J, Papenfuss AT, Baum B, Speed TP, Cowman AF. Regulation of apicomplexan
807 actin-based motility. Nat Rev Microbiol [Internet]. 2006;4(8):621–8. Available from:
808 http://www.ncbi.nlm.nih.gov/pubmed/16845432

809 77. Sangare LO, Alayi TD, Westermann B, Hovasse A, Sindikubwabo F, Callebaut I, et al.
810 Unconventional endosome-like compartment and retromer complex in Toxoplasma gondii
811 govern parasite integrity and host infection. Nat Commun [Internet]. 2016;7:11191.
812 Available from: https://www.ncbi.nlm.nih.gov/pubmed/27064065

813 78. Mueller C, Samoo A, Hammoudi PM, Klages N, Kallio JP, Kursula I, et al. Structural and
814 functional dissection of Toxoplasma gondii armadillo repeats only protein (TgARO). J Cell
815 Sci [Internet]. 2016; Available from: http://www.ncbi.nlm.nih.gov/pubmed/26769898

816 79. Roos DS, Donald RG, Morrissette NS, Moulton AL. Molecular tools for genetic dissection
817 of the protozoan parasite Toxoplasma gondii. Methods Cell Biol [Internet]. 1994;45:27–
818 63. Available from: http://www.ncbi.nlm.nih.gov/pubmed/7707991

819 80. Messina M, Niesman I, Mercier C, Sibley LD. Stable DNA transformation of Toxoplasma
820 gondii using phleomycin selection. Gene. 1995;

821 81. Robibaro B, Stedman TT, Coppens I, Ngô HM, Pypaert M, Bivona T, et al. Toxoplasma
822 gondii Rab5 enhances cholesterol acquisition from host cells. Cell Microbiol. 2002;

82. Whitelaw JA, Latorre-Barragan F, Gras S, Pall GS, Leung JM, Heaslip A, et al. Surface attachment, promoted by the actomyosin system of Toxoplasma gondii is important for efficient gliding motility and invasion. BMC Biol. 2017;15(1):1–23.

83. Lord SJ, Velle KB, Mullins RD, Fritz-Laylin LK. SuperPlots: Communicating reproducibility and variability in cell biology. J Cell Biol. 2020;

Figure legends:

Figure 1. Rab6 and syntaxin 6 co-localize to the same post-Golgi compartment. (A) Schematic diagram of the endomembrane system in *T. gondii*. (B). RH parasites expressing Grasp55-mcherry (Golgi marker; yellow) and NeonFP-Rab5 (magenta; upper panel) or (EmGFP-Rab6 (magenta; lower panel) were fixed and stained with DAPI (cyan). (C) RH parasites expressing AppleFP-Rab6 (magenta; all panels) with markers of the endomembrane system as indicated (yellow). Nuclei were stained with DAPI (cyan). Panels i-iii are deconvolved images of a single focal plane from fixed intracellular parasites. Panels iv-v are a single focal plane from live intracellular parasites expressing AppleFP-Rab6 (magenta) and SAG1ΔGPI-GFP (marker for the dense granules) or Syn6-GFP respectively. Panel vi is a single extracellular parasite expressing AppleFP-Rab6 that fixed and stained with an anti-CPL antibody and DAPI. Scale bar = 5µm. Inset scale bar in panel iv is 1µm.

Figure 2. The Rab6 and syntaxin 6 PGC is dynamic. (A) Live imaging of RH parasites expressing AppleFP-Rab6 and Syn6-GFP. Rab6 vesicles indicated with the arrow head. Areas in the white box were used to make inset images in panels (B) and (C). Scale bar = 5µm. (B) Upper panel. Inset 1 from panel (A). Dashed line was used to make line scan in lower panel. Bracket indicates Rab6 positive and Syn6 negative tubule. Magenta arrow indicates vesicular compartment containing both Rab6 and Syn6. Lower panel. Line scan of Rab6 and Syn6. Shift in peaks between Rab6 and Syn6 likely due to sequential image acquisition between the two imaging channels. Scale bar is 1µm. (C) Left panel. Image from Inset 2 from panel (A), taken at times indicated. Bracket indicates Rab6 positive and Syn6 negative tubule. Magenta arrow indicates vesicular compartment containing both Rab6 and Syn6. Dashed lines were used to make line scan in right panel. Right panel. Line scans of Rab6 and Syn6 at times indicated. Scale bar is 1µm.

Figure 3. **Rab6 vesicle transport is actin dependent**. (A-B) *Left panel*. RH parasites expressing EmGFP-Rab6 treated with DMSO (A) or cytochalasin D (CD) (B). Dashed oval indicates the PV surrounding a 2-parasite vacuole. Location of the nucleus is indicated by the blue circles. Area in the yellow box was used to make inset (middle panel). Arrow indicates parasite's apical end. *Middle panel.* Rab6 compartment dynamics. Images taken at 5 second intervals. *Right panel*. Kymograph depicting Rab6 directed vesicle motion. No directed motion was observed after cytochalasin D treatment. (C) Number of Rab6 vesicles per parasite was quantified in DMSO and CD treated parasites. (D) Number of directed runs/parasite/minute (run frequency) observed in DMSO and CD treated parasites. In (C) and (D) results are from three independent experiments. Mean from each independent experiment is indicated with large

circles. Raw data is shown with smaller colored circles. Experiment 1 in magenta, experiment 2 in cyan, experiment 3 in grey. Error bars indicated mean and SEM.

Figure 4. **Creation of TgMyoF-KD parasites using the auxin-inducible degradation system.** (A) Cartoon of TgMyoF knockdown strategy. (B) Western blot analysis of TgMyoF-AID-HA depletion as a function of IAA treatment time. Tubulin was used as the loading control. (C) Deconvolved epifluorescence images of TgMyoF-AID parasites treated with EtOH or IAA for 15 hours before fixation. Anti-HA immunofluorescence (magenta) was used to assess TgMyoF depletion. Anti-IMC1 antibody (green) and DAPI (cyan) staining used to visualize the parasite periphery and nuclei respectively.

Figure 5. **TgMyoF knockdown results in fragmentation and dispersion of post-Golgi compartments**. (A) TgMyoF-AID parasites expressing Neon-Rab5, EmGFP-Rab6, Neon-Rab7, GFP-Syn6 or GFP-DrpB (magenta) were treated with EtOH (left panels) or IAA (right panels) for 18 hours before fixation. Parasites were stained with anti-IMC1 to highlight the parasite periphery (yellow) and DAPI to stain DNA (cyan). Scale bar is 5μm. (B) For each post-Golgi compartment, the number of objects was quantified in control and TgMyoF knockdown parasites. Combined results from two or three independent experiments. Mean from each independent experiment is indicated with large circles. Raw data is shown with smaller colored circles. Experiment 1 in magenta, experiment 2 in cyan, experiment 3 in grey. Error bars indicated mean and SEM. (C) TgMyoF-AID parasites expressing Syn6-GFP (yellow) and AppleFP-Rab6 (magenta) treated with EtOH (top row) or IAA (middle and bottom rows). *Bottom row.* Inset is magnification of area in the dashed box. Inset scale bar is 1μm.

Figure 6. TgMyoF is required for Rab6 vesicle transport. (A-B) *Left panel:* TgMyoF-AID parasites expressing EmGFP-Rab6 treated with EtOH (A) or IAA (B) for 18 hours before imaging. Dashed oval indicates the PV surrounding a 2-parasite vacuole. Location of the nucleus is indicated by the blue circles. Area in the yellow box was used to make inset (middle panel). *Middle panel:* Images of the Rab6 compartment taken at 5 second intervals. *Right panel:* Kymograph depicting Rab6 vesicle motion. (C) Run frequency (# of directed runs/parasite/minute) of Rab6 vesicles in control and TgMyoF depleted parasites. Combined results from two independent experiments. Mean from each independent experiment is indicated with large circles. Raw data is shown with smaller colored circles. Experiment 1 in magenta, experiment 2 in cyan. Error bars indicated mean and SEM. (D) Frequency distribution of Rab6 vesicle velocities in RH parasites (orange) and in TgMyoF-AID parasites treated with EtOH (blue) or IAA (green) for 18 hours.

Figure 7. TgMyoF is required for ER tubule movement. (A&B) *Left panel*: TgMyoF-AID parasites treated with EtOH (A) or IAA (B) where the ER is fluorescently labeled with eGFP. *Right panel:* magnification of area in the white box. First image of each movie (grey) was overlaid with images taken after 5s (magenta), 10s (yellow) and 15s (cyan) of imaging.

905 **Figure 8. TgMyoF and actin control Golgi morphology.** (A) Diagram of centrosome and golgi
906 division. (B) TgMyoF-AID parasites expressing mCherry-Grasp55 (a marker of the cis-Golgi;
907 magenta) were fixed and stained with anti-IMC1 (green) and DAPI (cyan) after 15 hours of
908 EtOH or IAA treatment. (C) TgMyoF-AID parasites expressing mCherry-Grasp55 were treated
909 with DMSO or CD for 60 minutes before fixation and DAPI staining. White arrows indicate Golgi
910 fragments. (D) Quantification of # of Golgi/parasite in TgMyoF-AID parasites treated with EtOH
911 for 15 hours (blue), IAA for 4 hours (dark green), IAA for 15 hours (light green) or CD for 60
912 minutes (orange). Results are combined data from at least 2 independent experiments. N>50
913 parasites/experiment. (E) Quantification of Golgi localization in apical only, basal only or both
914 the apical and basal ends of the parasite. Results are combined data from 2 independent
915 experiments. N>50 parasites/experiment. (F) TgMyoF-AID parasites expressing mCherry-
916 Grasp55 (magenta) and centrin 1-GFP (as a marker of the centrosome; yellow) were treated
917 with EtOH and IAA for 15 hours before fixation and DAPI staining. Arrowhead indicates the
918 centrosome. Arrows indicate the Golgi. (G) Quantification of centrosome and Golgi number in
919 control and TgMyoF depleted parasites. Combined results from 2 independent experiments.
920 N=77 parasites for control, N=93 parasites for IAA treated. (H) Centrosome number per
921 TgMyoF-AID parasite treated with EtOH or IAA. Combined results from 2 independent
922 experiments. N=77 parasites for control, N=93 parasites for IAA treated.

923

924 **Figure 9. TgMyoF depletion affects apical positioning of the rhoptries and Rop1 vesicle**
925 **movement.** (A) TgMyoF-AID parasites expressing Rop1-NeonFP (magenta) were treated with
926 EtOH and IAA for 15 hours before fixation and staining with an anti-AMA1 (green) and anti-
927 GAP45 (yellow) antibodies and DAPI (cyan). Magenta arrow indicates Rop1 vesicles in the
928 cytosol. Yellow arrow indicates the residual body (RB). (B) Quantification of TgMyoF-AID
929 parasites with micronemes (visualized with anti-AMA1 antibody) and rhoptries (visualized by
930 expression of Rop1-NeonFP) in the residual body. N = 57 vacuoles for AMA-1 quantitation,
931 N=77 vacuoles for Rop-1 quantitation from two independent experiments. (C&D) TgMyoF-AID
932 parasite's expressing Rop1-NeonFP were treated with EtOH or IAA for 15 hours before live cell
933 imaging. *Right panel:* Rop1 localization. Magenta arrow indicates rhoptry mislocalization to the
934 parasites basal end. White arrow indicates parasite apical end. Dashed oval indicates the PV in
935 a 2-parasite vacuole. Area in the white box was used to make inset in the left panel. *Left panel:*
936 Dynamics of rhoptries in the first 15 seconds of imaging. (E) Run frequency (# of directed
937 runs/parasite/minute) of Rop1 vesicles in control and TgMyoF depleted parasites. See table S1
938 for more details. (F) Number of Rop1 vesicles per parasite. N = 63 and 76 parasites in control
939 and TgMyoF-KD parasites respectively in 3 independent experiments. (G) Ratio of Rop1
940 fluorescence in the apical and basal ends of the parasite. N = 63 and 76 parasites in control and
941 TgMyoF-KD parasites respectively in 3 independent experiments. (E-G) Mean from each
942 independent experiment is indicated with large circles. Raw data is shown with smaller circles;
943 experiment 1 in magenta, experiment 2 in cyan, experiment 3 in grey. Error bars indicate mean
944 and SEM.

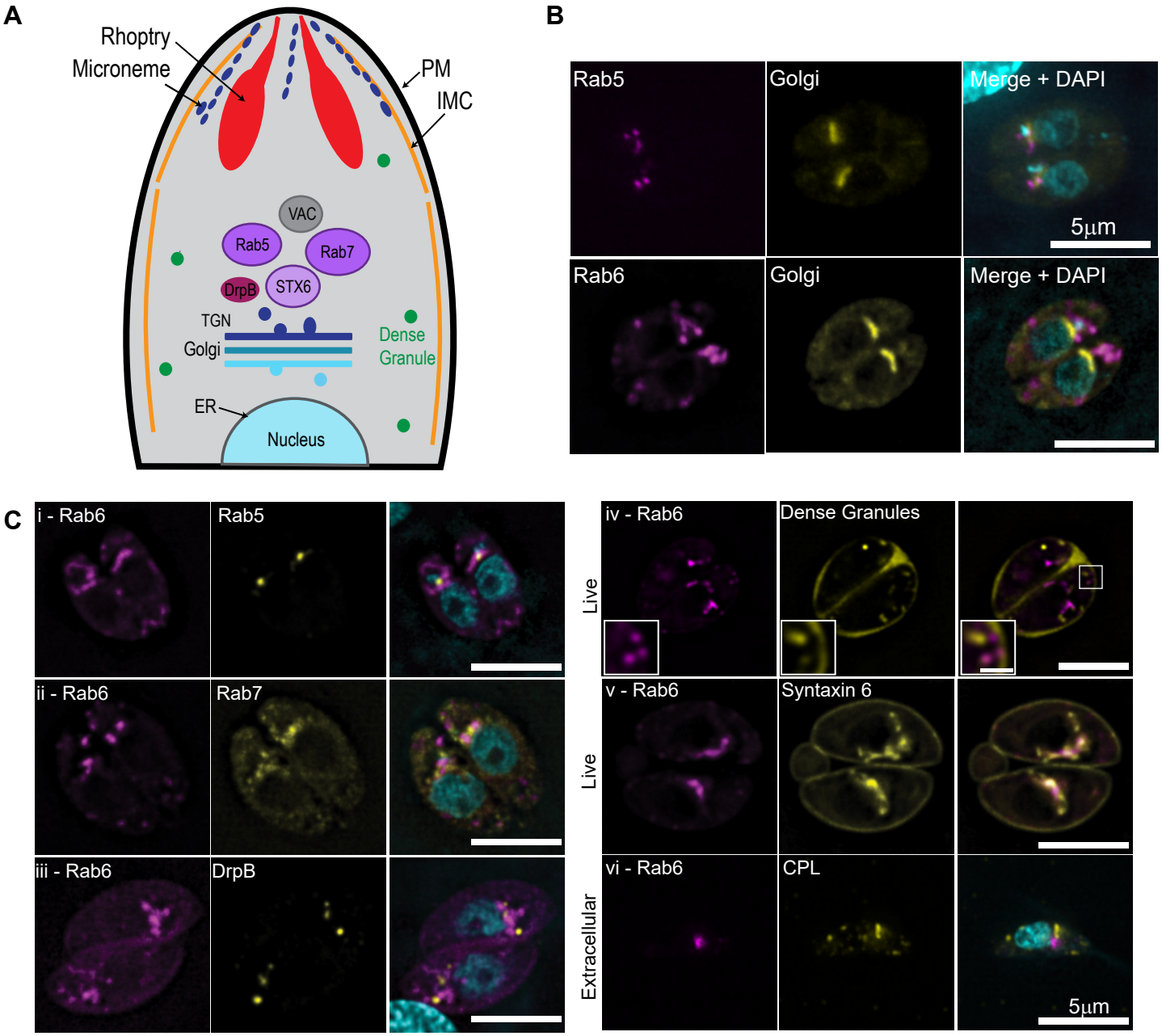
A
Rhoptry
Microneme
PM
IMC
VAC
Rab5
Rab7
DrpB
STX6
TGN
Golgi
Dense
Granule
ER
Nucleus
B
Rab5
Golgi
Merge + DAPI
5µm
Rab6
Golgi
Merge + DAPI
C
i - Rab6
Rab5
ii - Rab6
Rab7
iii - Rab6
DrpB
Live
iv - Rab6
Dense Granules
Live
v - Rab6
Syntaxin 6
Extracellular
vi - Rab6
CPL
5µm

Figure 1.

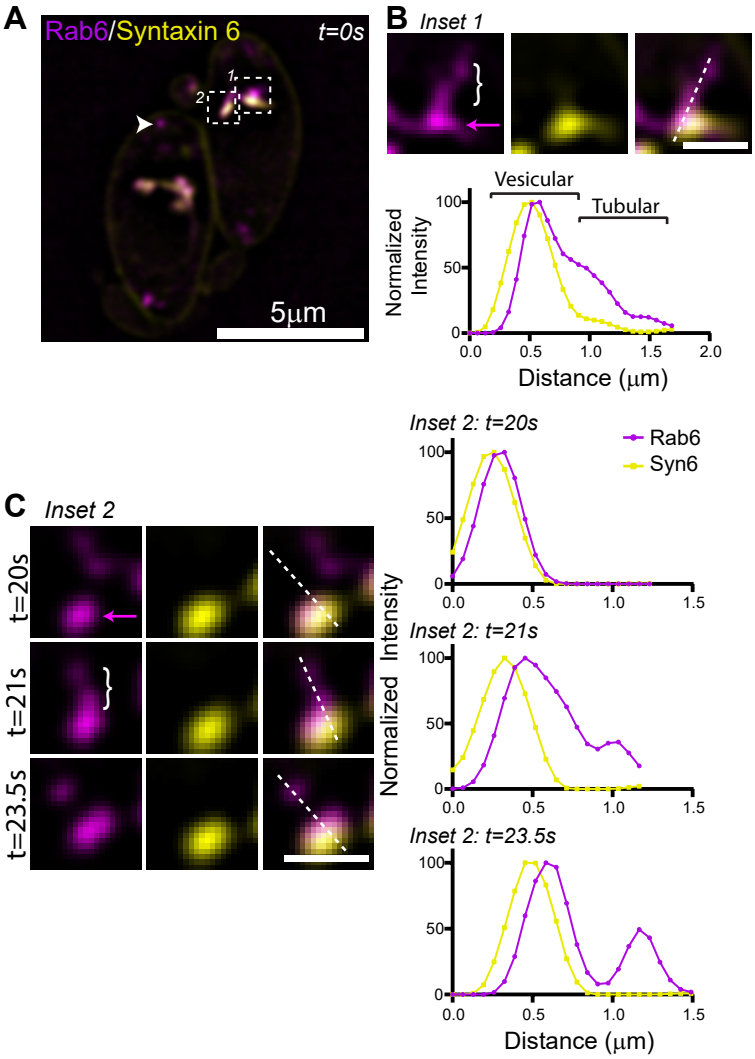
A
Rab6/Syntaxin 6
t=0s
1
2
5µm
B
Inset 1
Vesicular
Tubular
Normalized Intensity
Distance (µm)
C
Inset 2
t=20s
t=21s
t=23.5s
Inset 2: t=20s
Inset 2: t=21s
Inset 2: t=23.5s
Rab6
Syn6
Normalized Intensity
Distance (µm)

Figure 2.

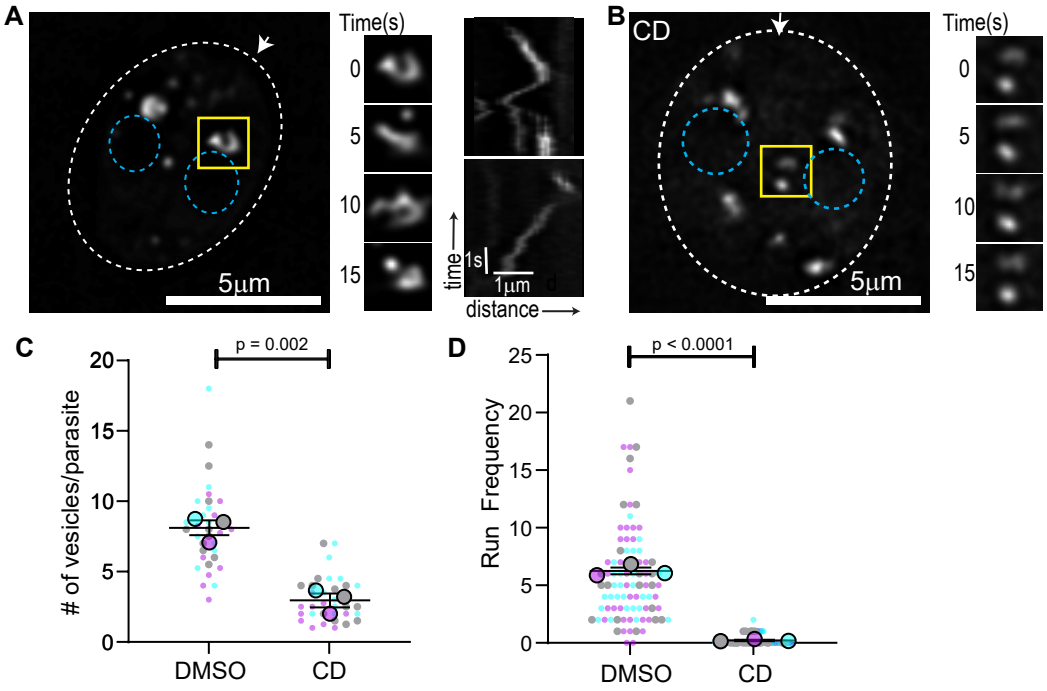
A
Time(s)
0
5
10
15
5µm
time
1s
1µm
distance
B
CD
Time(s)
0
5
10
15
5µm
C
p = 0.002
# of vesicles/parasite
20
15
10
5
0
DMSO
CD
D
p < 0.0001
Run Frequency
25
20
15
10
5
0
DMSO
CD

Figure 3.

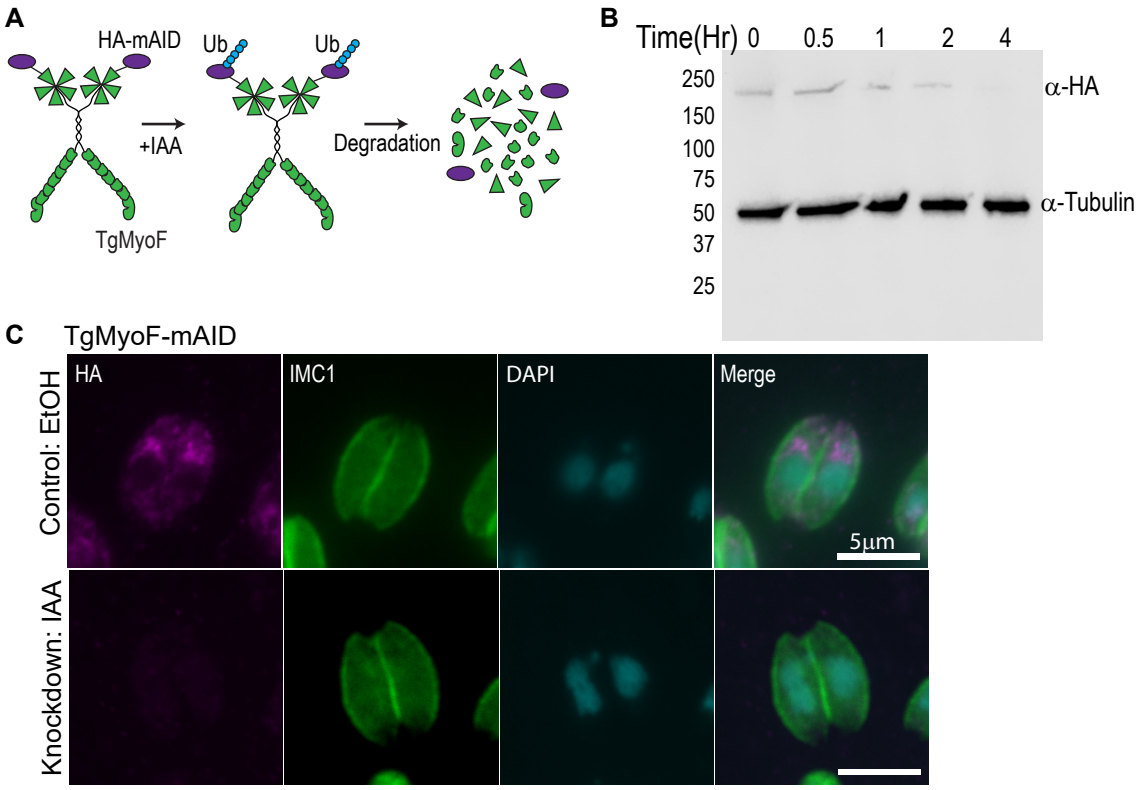
A
HA-mAID
Ub
Ub
+IAA
Degradation
TgMyoF
B
Time(Hr) 0 0.5 1 2 4
250
150
100
75
50
37
25
α-HA
α-Tubulin
C
TgMyoF-mAID
Control: EtOH
Knockdown: IAA
HA
IMC1
DAPI
Merge
5μm

Figure 4.

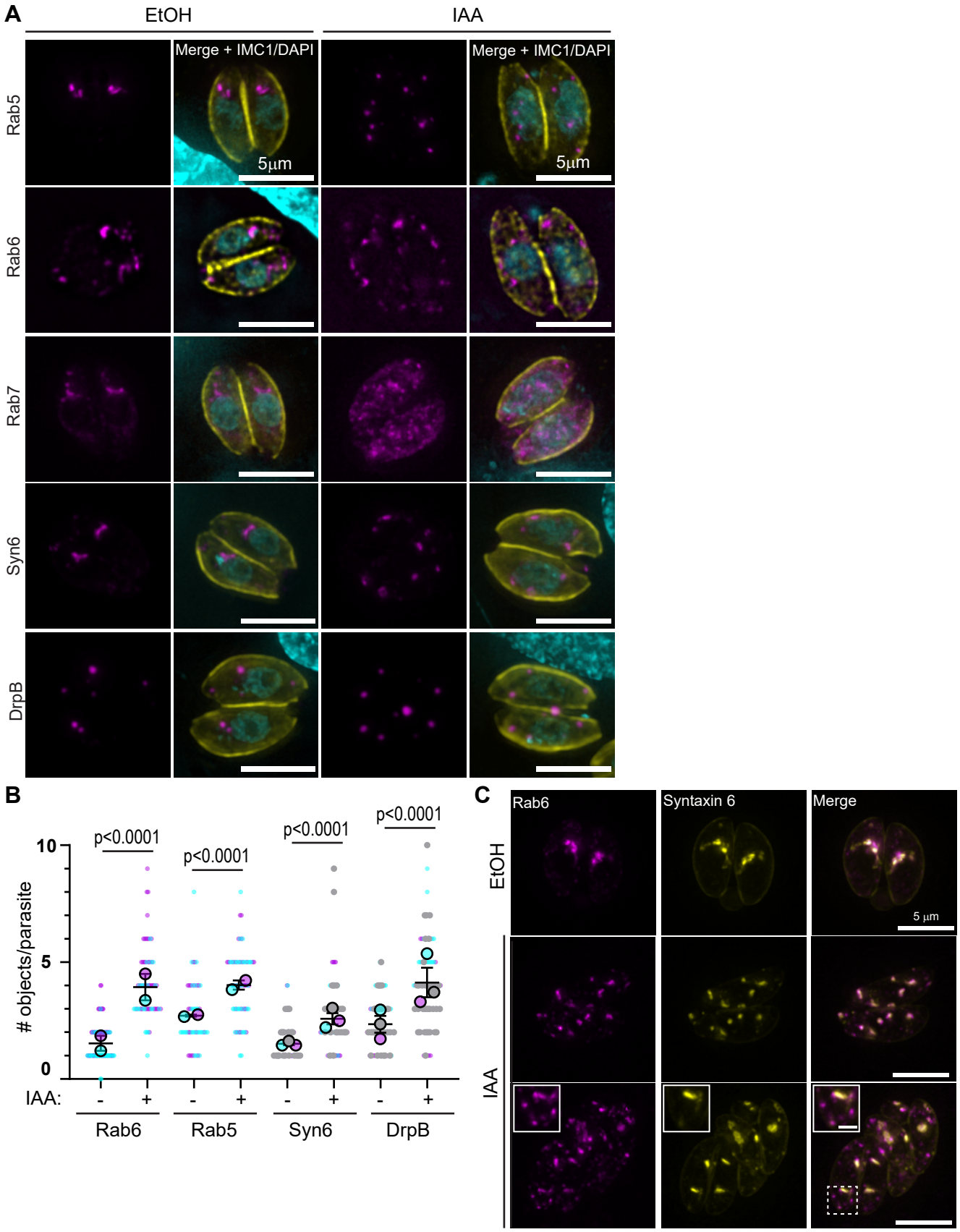
A
EtOH
IAA
Merge + IMC1/DAPI
Merge + IMC1/DAPI
5µm
5µm
Rab5
Rab6
Rab7
Syn6
DrpB
B
p<0.0001
p<0.0001
p<0.0001
p<0.0001
10
5
0
objects/parasite
IAA:
-
+
-
+
-
+
-
+
Rab6
Rab5
Syn6
DrpB
C
Rab6
Syntaxin 6
Merge
EtOH
IAA
5 µm

Figure 5.

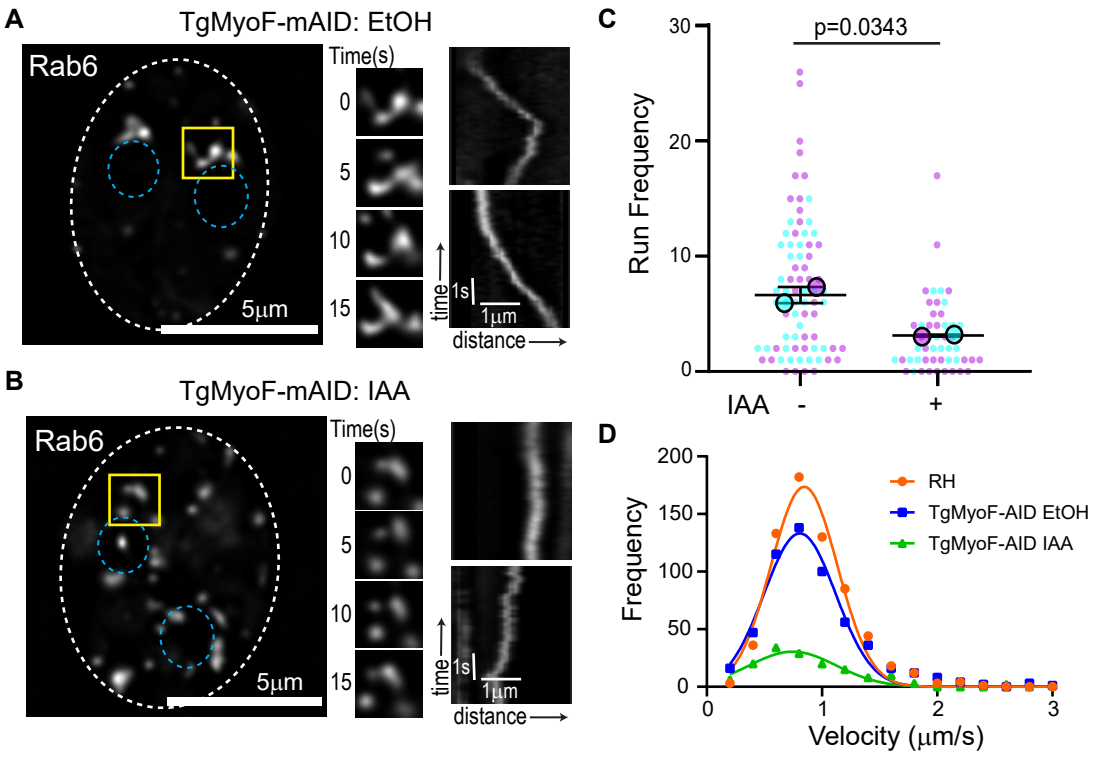
A
TgMyoF-mAID: EtOH
Rab6
Time(s)
0
5
10
15
5µm
time
1s
1µm
distance
B
TgMyoF-mAID: IAA
Rab6
Time(s)
0
5
10
15
5µm
time
1s
1µm
distance
C
p=0.0343
Run Frequency
30
20
10
0
IAA
-
+
D
Frequency
200
150
100
50
0
0
1
2
3
Velocity (µm/s)
RH
TgMyoF-AID EtOH
TgMyoF-AID IAA

Figure 6.

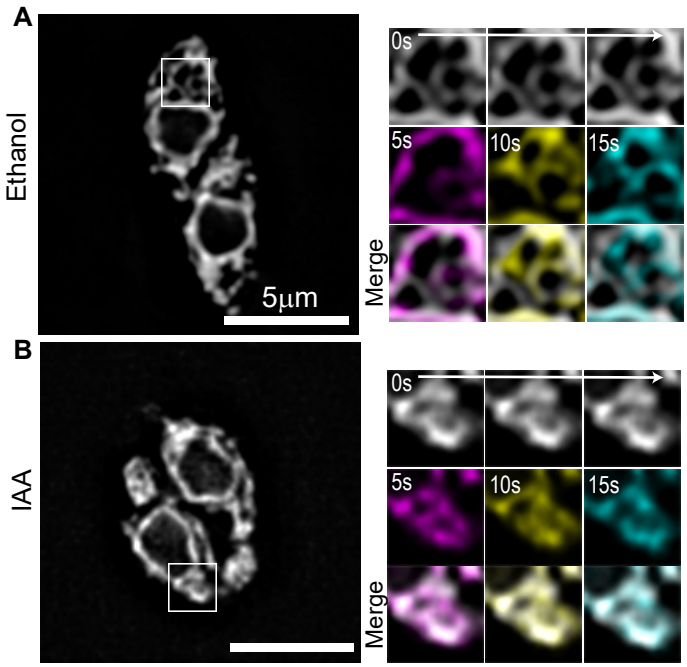

Figure 7.

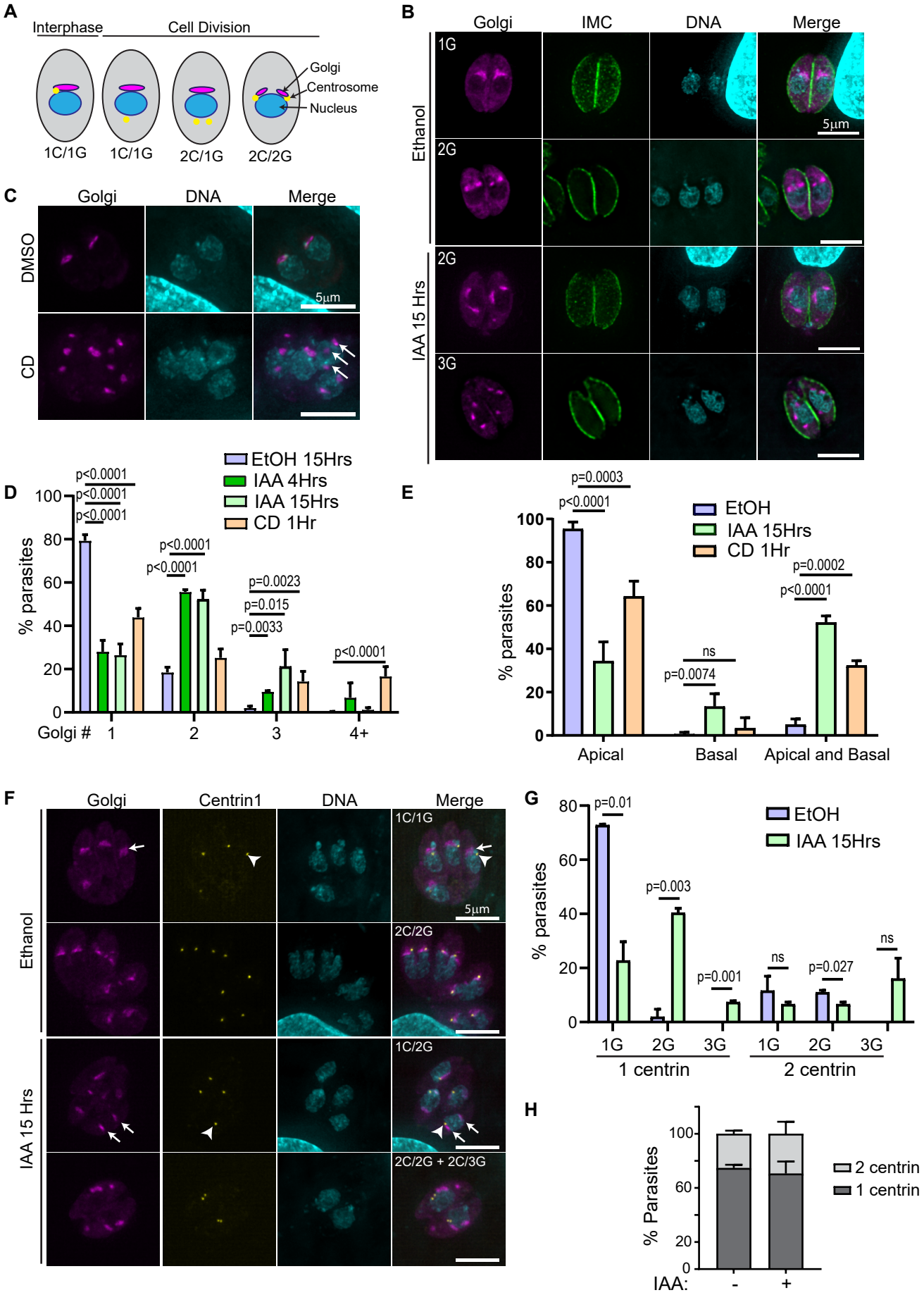
A
Interphase
Cell Division
Golgi
Centrosome
Nucleus
1C/1G
1C/1G
2C/1G
2C/2G
B
Golgi
IMC
DNA
Merge
Ethanol
IAA 15 Hrs
1G
2G
2G
3G
5µm
C
Golgi
DNA
Merge
DMSO
CD
5µm
D
EtOH 15Hrs
IAA 4Hrs
IAA 15Hrs
CD 1Hr
% parasites
Golgi #
1
2
3
4+
p<0.0001
p=0.0023
p=0.015
p=0.0033
E
EtOH
IAA 15Hrs
CD 1Hr
% parasites
Apical
Basal
Apical and Basal
p=0.0003
p<0.0001
ns
p=0.0074
p=0.0002
p<0.0001
F
Golgi
Centrin1
DNA
Merge
Ethanol
IAA 15 Hrs
1C/1G
2C/2G
1C/2G
2C/2G + 2C/3G
5µm
G
EtOH
IAA 15Hrs
% parasites
p=0.01
p=0.003
p=0.001
ns
p=0.027
ns
1G
2G
3G
1 centrin
2 centrin
H
% Parasites
2 centrin
1 centrin
IAA:
-
+

Figure 8.

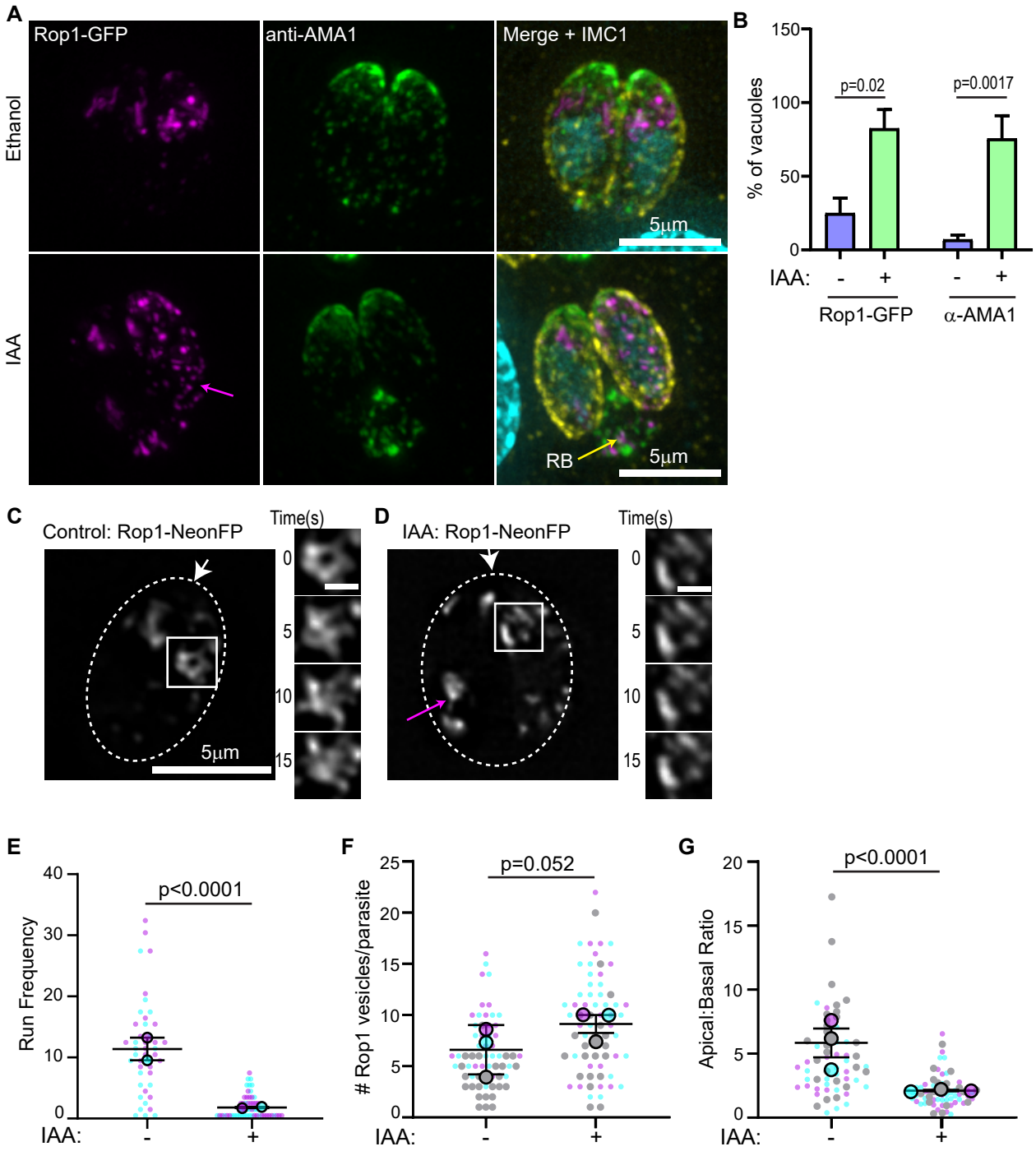
A
Rop1-GFP
anti-AMA1
Merge + IMC1
Ethanol
IAA
5µm
RB
B
% of vacuoles
p=0.02
p=0.0017
IAA:
Rop1-GFP
α-AMA1
C
Control: Rop1-NeonFP
Time(s)
D
IAA: Rop1-NeonFP
E
Run Frequency
p<0.0001
F
# Rop1 vesicles/parasite
p=0.052
G
Apical:Basal Ratio
p<0.0001

Figure 9.